

Supporting Information

Emergence of uniform tilt and π -stacking in triangular liquid crystalline honeycombs

Marco Poppe,^a Changlong Chen,^b Feng Liu,^{*,b} Silvio Poppe,^a and Carsten Tschierske^{*,a}

[a] Department of Chemistry, Martin-Luther-University Halle-Wittenberg, Kurt-Mothes Str.
2, D-06108 Halle/Saale, Germany

E-mail: carsten.tschierske@chemie.uni-halle.de

[b] State Key Laboratory for Mechanical Behaviour of Materials, Shaanxi International
Research Center for Soft Matter, Xi'an Jiaotong University, Xi'an 710049, P. R. China

E-mail: feng.liu@xjtu.edu.cn

1. Methods

Optical Polarizing Microscopy (POM). - Transition temperatures were measured using a Mettler FP-82 HT hot stage and control unit in conjunction with a Leica DMRXP polarizing microscope. Textures of the liquid crystalline mesophases were recorded with Leica MC120 HD camera.

DSC measurements. - Transition enthalpies were determined as obtained from DSC-thermograms which were recorded on a Perkin-Elmer DSC-7 (heating and cooling rate: 10 K/min).

X-ray scattering on powder-like and aligned samples. - X-ray investigations were carried out at Cu K_{α} line ($\lambda = 1.54 \text{ \AA}$) using a standard Coolidge tube source with a Ni-filter. The diffraction patterns were recorded with a 2D detector (Vantec 500, Bruker, Billerica, MA, USA), and the exposure time was 15 min for WAXS and 30 min for SAXS. Powder-like samples were prepared in 1 mm capillaries, the samples were held in a temperature-controlled oven, and the distance between the sample and the detector was 9.5 cm (WAXS) or 27.4 cm (SAXS). For aligned samples, a droplet of the sample on a glass substrate placed on a temperature-controlled heating stage was investigated. The droplets were prepared in the isotropic state and then cooled (rate: 1 K/min) to the measuring temperature. The distance between the sample and the detector was 9.0 cm (WAXS) or 26.8 cm (SAXS), and the beam was parallel to the substrate.

Synchrotron X-ray diffraction and electron density reconstruction. - High-resolution small-angle and wide-angle powder X-ray scattering experiments were recorded on Beamline BL16B1 at Shanghai Synchrotron Radiation Facility, SSRF. Samples were held in evacuated 1 mm capillaries. A Linkam hot stage with a thermal stability within 0.2 °C was used, with a hole for the capillary drilled through the silver heating block and mica windows attached to it on each side. A MarCCD detector was used. q calibration and linearization were verified using several orders of layer reflections from silver behenate and a series of n -alkanes. The measurement of the positions and intensities of the diffraction peaks is carried out using program, where experimental diffractograms are fitted using Gaussian shaped peaks. The diffraction peaks are indexed on the basis of their peak positions, and the lattice parameters and the plane/space groups are subsequently determined. Once the diffraction intensities are

measured and the corresponding plane group determined, 2-*d* electron density maps can be reconstructed, on the basis of the general formula

$$E(xy) = \sum_{hkl} F(hk) \exp[i2\pi(hx+ky)] \quad (\text{Eqn. 1})$$

Here $F(hk)$ is the structure factor of a diffraction peak with index (hk) . It is normally a complex number and the experimentally observed diffraction intensity

$$I(hk) = K \cdot F(hk) \cdot F^*(hk) = K \cdot |F(hk)|^2 \quad (\text{Eqn. 2})$$

Here K is a constant related to the sample volume, incident beam intensity etc. In this paper we are only interested in the relative electron densities, hence this constant is simply taken to be 1.

Thus, the electron density

$$E(xy) = \sum_{hkl} \sqrt{I(hk)} \exp[i2\pi(hx+ky) + \phi_{hk}] \quad (\text{Eqn. 3})$$

As the observed diffraction intensity $I(hk)$ is only related to the amplitude of the structure factor $|F(hk)|$, the information about the phase of $F(hk)$, ϕ_{hk} , can not be determined directly from experiment. However, the problem is much simplified when the structure of the ordered phase is centrosymmetric, and hence the structure factor $F(hk)$ is always real and ϕ_{hk} is either 0 or π .

This makes it possible for a trial-and-error approach, where candidate electron density maps are reconstructed for all possible phase combinations, and the “correct” phase combination is then selected on the merit of the maps, helped by prior physical and chemical knowledge of the system. This is especially useful for the study of nanostructures, where normally only a limited number of diffraction peaks are observed.

2. Additional Data

2.1 DSC data and phase transitions

Table S1. Mesophases, transition temperatures and associated enthalpy values of compounds **H_n** on heating (*H:*) and cooling (*C:*) determined by DSC (10 K·min⁻¹, peak temperatures)^[S1]

Comp.	<i>n</i>	Phase transitions <i>T</i> /°C [ΔH /kJ mol ⁻¹]
H6^a	6	<i>H:</i> Cr 111 [27.0] Col _{hex} 178 [4.5] Iso <i>C:</i> Iso 176 [-4.6] Col _{hex} 74 [-5.4] Cr
H8	8	<i>H:</i> Cr 77 [21.0] Col _{hex} ^{<i>T</i>(Δ)} 80 [0.7] Col _{hex(Δ)} 185 [7.7] Iso <i>C:</i> Iso 183 [-7.8] Col _{hex(Δ)} 76 [-0.7] Col _{hex} ^{<i>T</i>(Δ)} 60 [-16.3] Iso
H10	10	<i>H:</i> Cr 61 [19.6] (Col _{hex} ^{<i>T</i>(Δ)} 55 [0.2]) Col _{hex(Δ)} 185 [11.0] Iso <i>C:</i> Iso 182 [-11.6] Col _{hex(Δ)} 50 [-0.2] Col _{hex} ^{<i>T</i>(Δ)} 38 [-12.6] Cr
H12	12	<i>H:</i> Cr 97 [70.1] Col _{hex(Δ)} 175 [11.9] Iso <i>C:</i> Iso 173 [-12.4] Col _{hex(Δ)} 23 [-18.9] Cr

^a An additional low temperature M1 phase, as reported in ref. S1, can be excluded based on repeated optical and DSC investigations.

Table S2. Mesophases, transition temperatures and associated enthalpy values of compounds **F_n** on heating (*H:*) and cooling (*C:*) determined by DSC (10 K·min⁻¹, peak temperatures).

F_n	<i>n</i>	Phase transitions /°C [ΔH /kJ mol ⁻¹]
F6	6	<i>H:</i> Cr 165 [23.2] Col _{hex} 179 [6.2] Iso <i>C:</i> Iso 177 [-6.3] Col _{hex} 158 [-16.8] Cr
F8	8	<i>H:</i> Cr 151 [0.6] (Col _{hex} ^{<i>T</i>(Δ)} 149 [1.2]) Col _{hex(Δ)} 191 [12.5] Iso <i>C:</i> Iso 188 [-12.9] Col _{hex(Δ)} 149 [-1.2] Col _{hex} ^{<i>T</i>(Δ)} < 20 Cr
F10	10	<i>H:</i> Cr 74 [1.4] (Col _{hex} ^{<i>T</i>(Δ)} 62 [0.01]) Col _{hex(Δ)} 189 [19.4] Iso <i>C:</i> Iso 187 [-21.2] Col _{hex(Δ)} 58 [-0.01] Col _{hex} ^{<i>T</i>(Δ)} < 20 Cr
F12	12	<i>H:</i> Cr 73 [79.3] Col _{hex(Δ)} 182 [19.2] Iso <i>C:</i> Iso 182 [-18.1] Col _{hex(Δ)} < 20 Cr

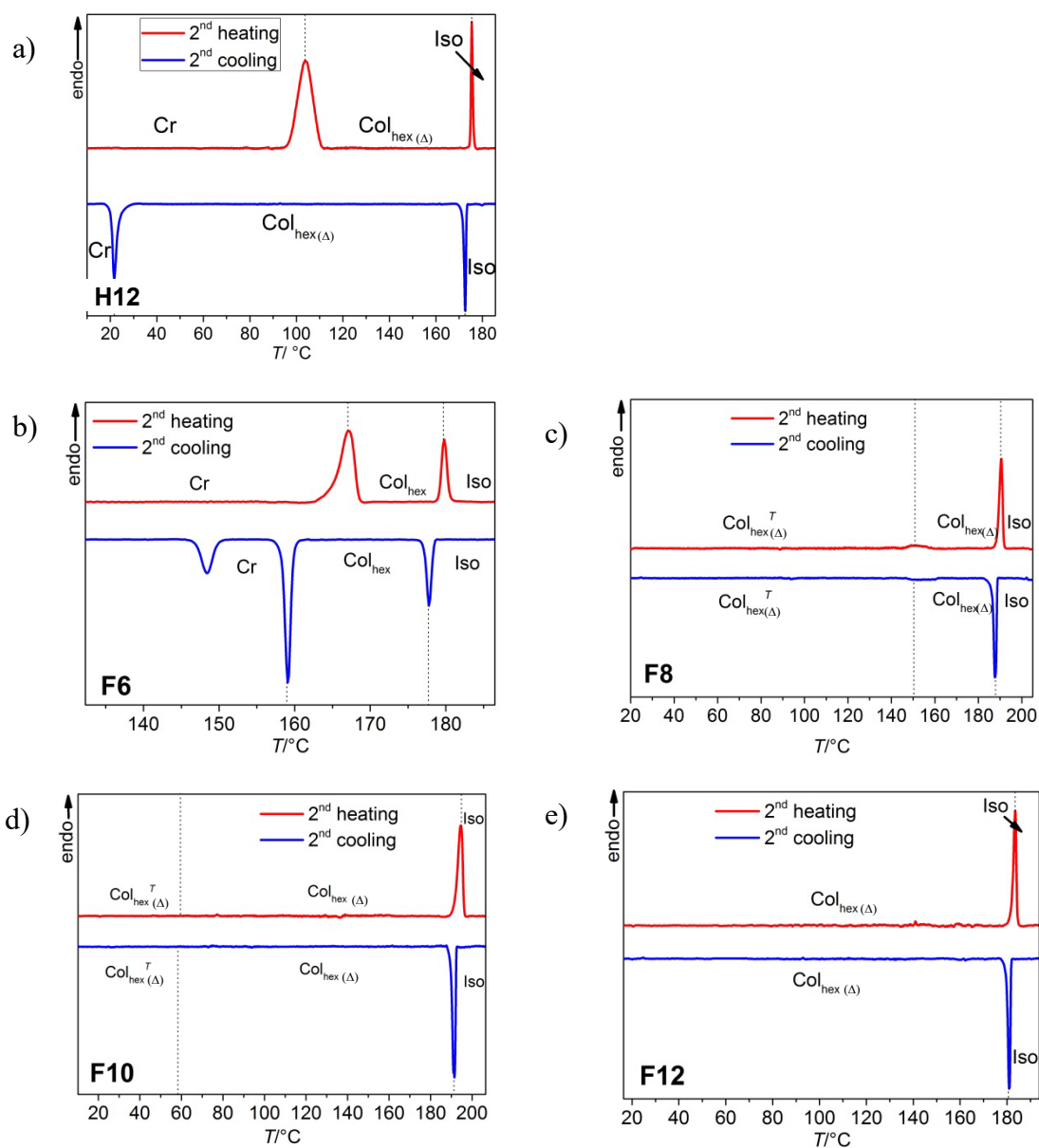


Figure S1. DSC heating and cooling traces of compounds **H12** and **F n** recorded at 10 K/min; for DSCs of the other compounds **H n** , see ref. S1.

2.2 Additional textures

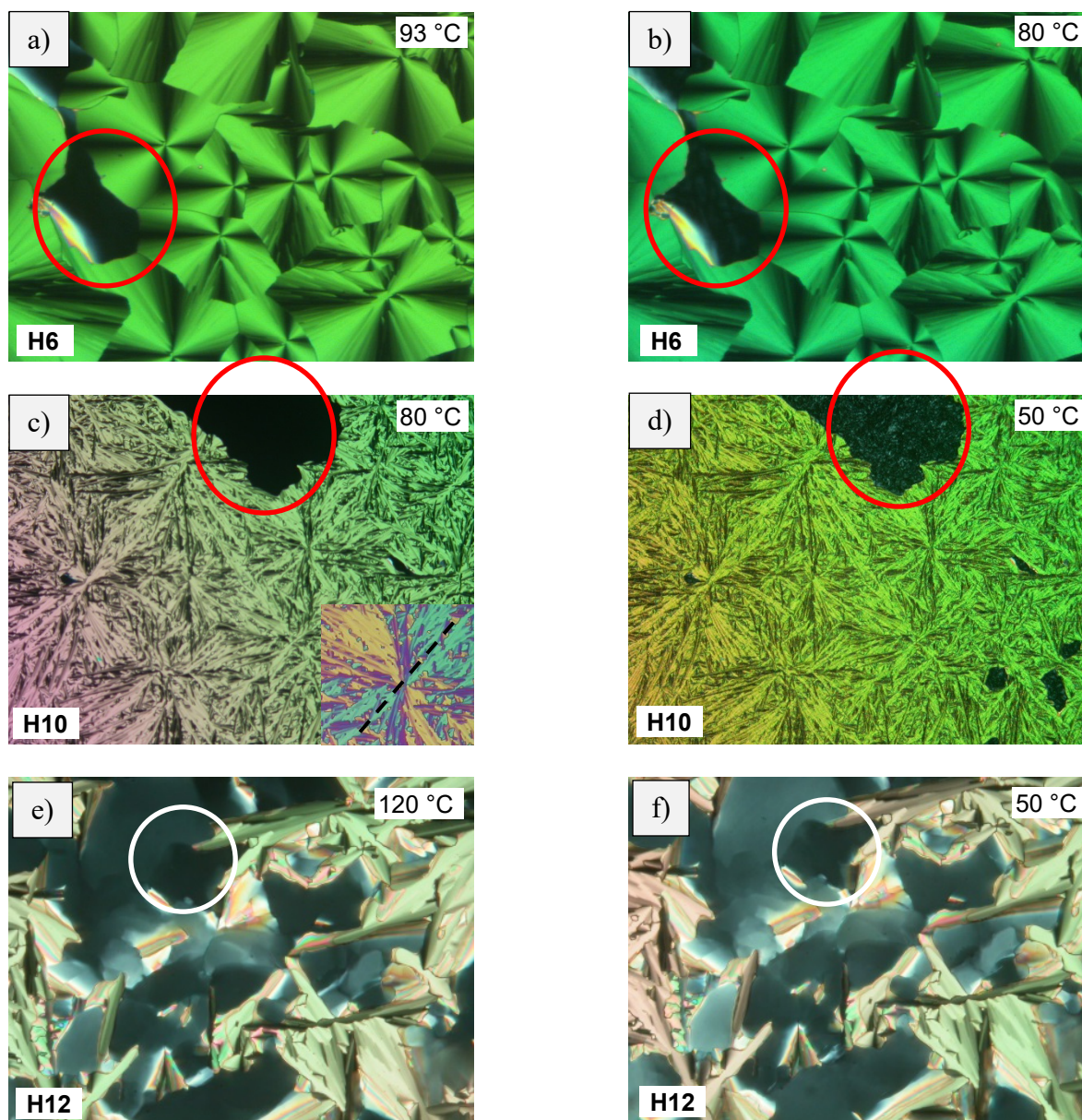


Figure S2. Textures of the $\text{Col}_{\text{hex}}/\text{Col}_{\text{hex}(\Delta)}/\text{Col}_{\text{hex}}^{T(\Delta)}$ phases of selected compounds **Hn** as observed between crossed polarizers. a, b) Col_{hex} phase of compound **H6**, a) at 93 °C and b) at 80 °C, indicating no change of the texture, especially the optically isotropic homeotropic areas (encircled; columns are perpendicular to the substrate surface) remain dark; c, d) $\text{Col}_{\text{hex}(\Delta)} - \text{Col}_{\text{hex}}^{T(\Delta)}$ transition of compound **H10**; c) shows the optical negative spherulitic texture at 80 °C (inset shows texture with λ -retarder plate, the slow axis direction is indicated by dotted line) and d) at 50 °C. The orientation of the blue shifted areas being oriented NE and SW with λ -retarder plate indicates negative birefringence as typical for honeycomb phases. At the phase transition $\text{Col}_{\text{hex}(\Delta)}/\text{Col}_{\text{hex}}^{T(\Delta)}$ the birefringence in the birefringent (planar aligned regions with the columns parallel to the substrate surfaces) is reduced (red to yellow on the left-hand side) and the dark homeotropic regions (encircled) in c) become birefringent in d), indicating the transition to a synclinic tilted honeycomb; e, f) $\text{Col}_{\text{hex}(\Delta)}$ phase of compound **H12** e) at $T = 120$ °C and f) at $T = 50$ °C; the dark homeotropic areas (encircled) remain dark, indicating the absence of a synclinic tilted phase. The birefringence color change

in the planar areas from green to red (left side) indicating an increasing birefringence in this case, which is in line with the growing orientational order with decreasing T .

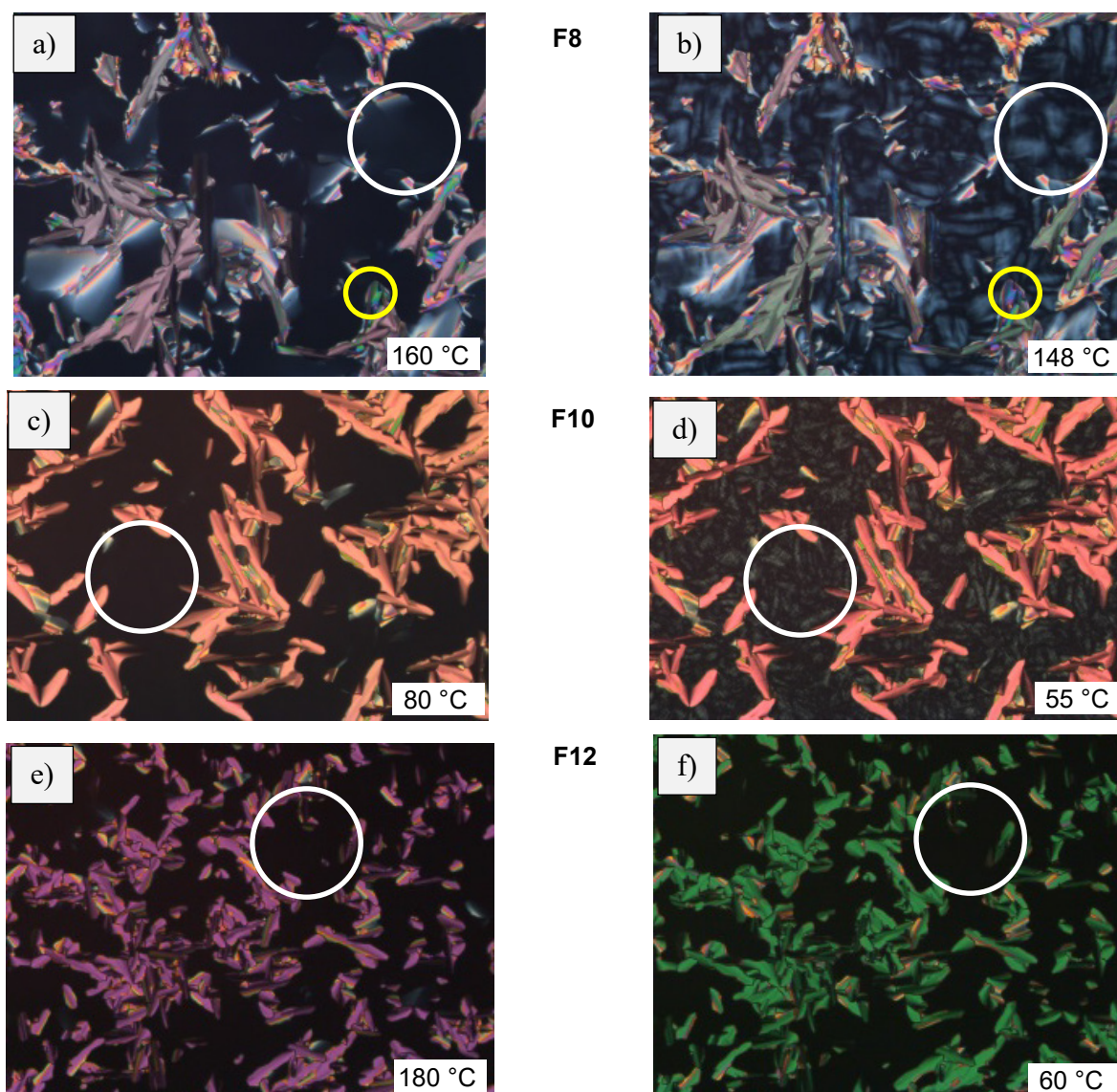


Figure S3. Textures of the transition from non-tilted to tilted organization of the fluorinated compounds **F n** . a-d) shows the transition $\text{Col}_{\text{hex}(\Delta)} - \text{Col}_{\text{hex}^T(\Delta)}$ of a, b) **F8** from a) 160 °C to b) 148 °C. At the phase transition the birefringence decreases in the planar aligned areas (green to blue in yellow circles) and the homeotropic regions become birefringent (white circles), in line with the onset of a synclitic tilt. c, d) show the same transition of compound **F10** from c) 80 °C to d) 55 °C. e, f) show the textures of the $\text{Col}_{\text{hex}(\Delta)}$ phase of compound **F12** at e) 180 °C and f) 60 °C. Because no tilt develops, there is no onset of a birefringence in the homeotropic regions (encircled); the increasing order parameter leads to an increase of birefringence (violet to green) in the planar aligned areas with lowering temperature.

2.3 Additional SAXS data

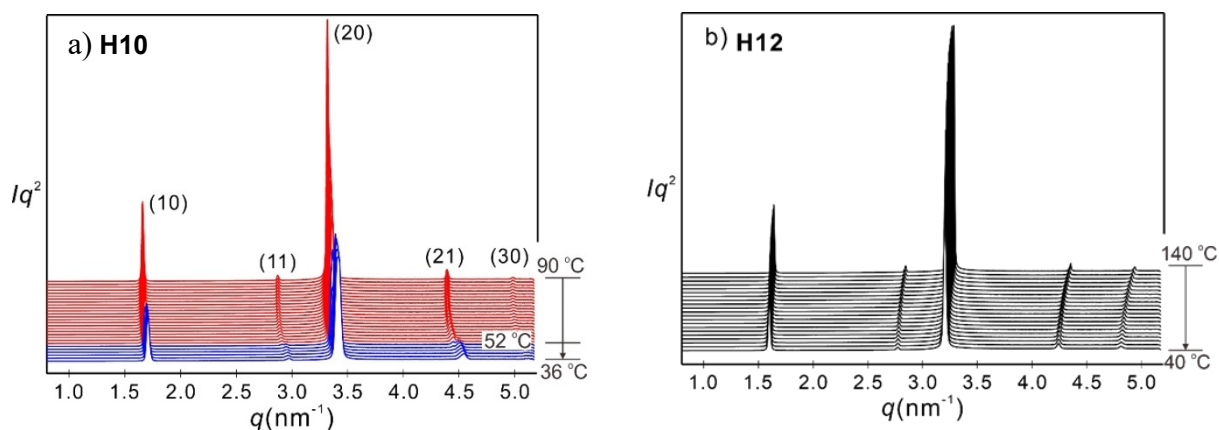


Figure S4. Temperature-dependence of the SAXS diffractograms of compounds a) **H10** and b) **H12**.

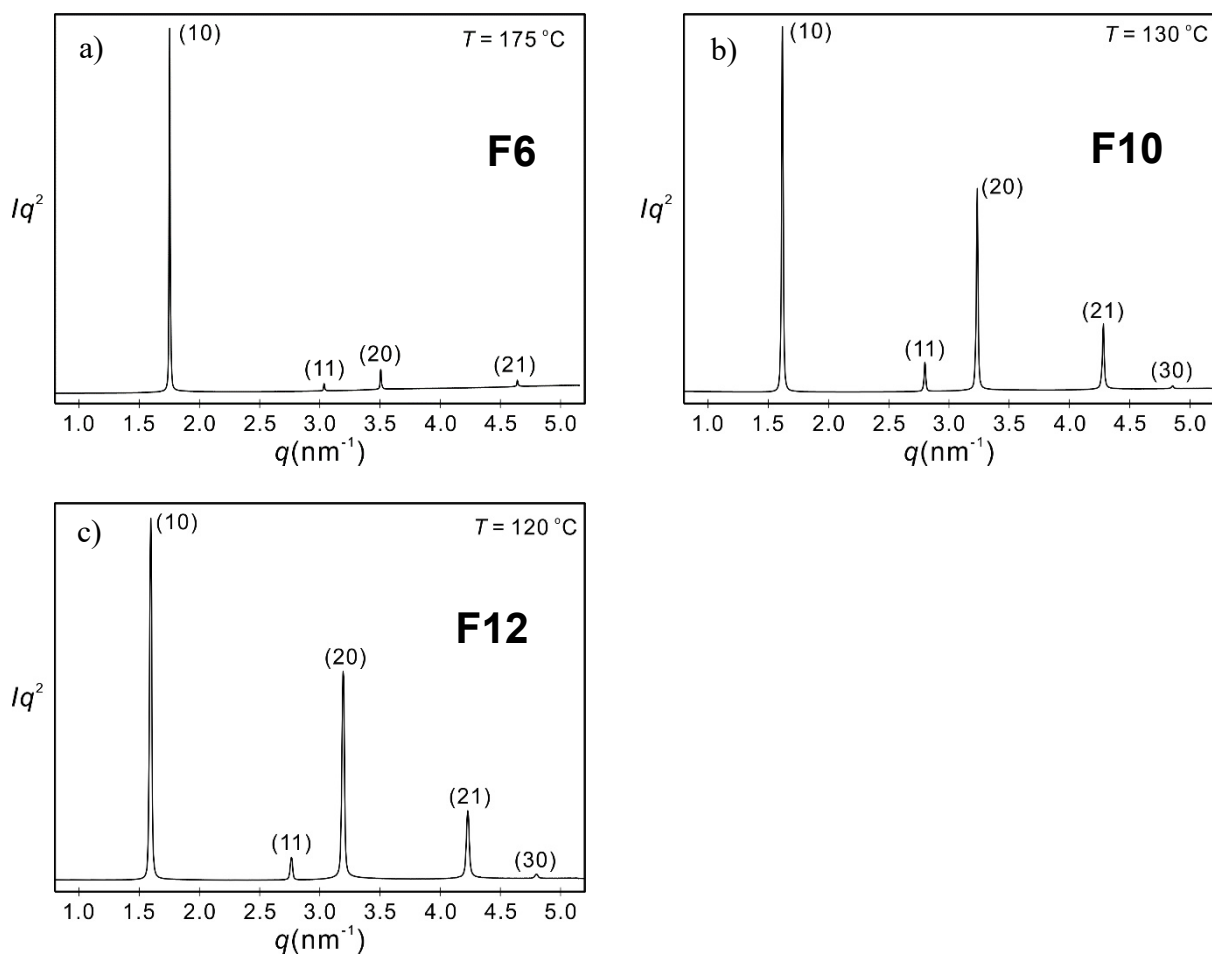


Figure S5. SAXS diffractogram of the $\text{Col}_{\text{hex}(\Delta)}$ phases of selected compounds **F_n** at given temperatures.

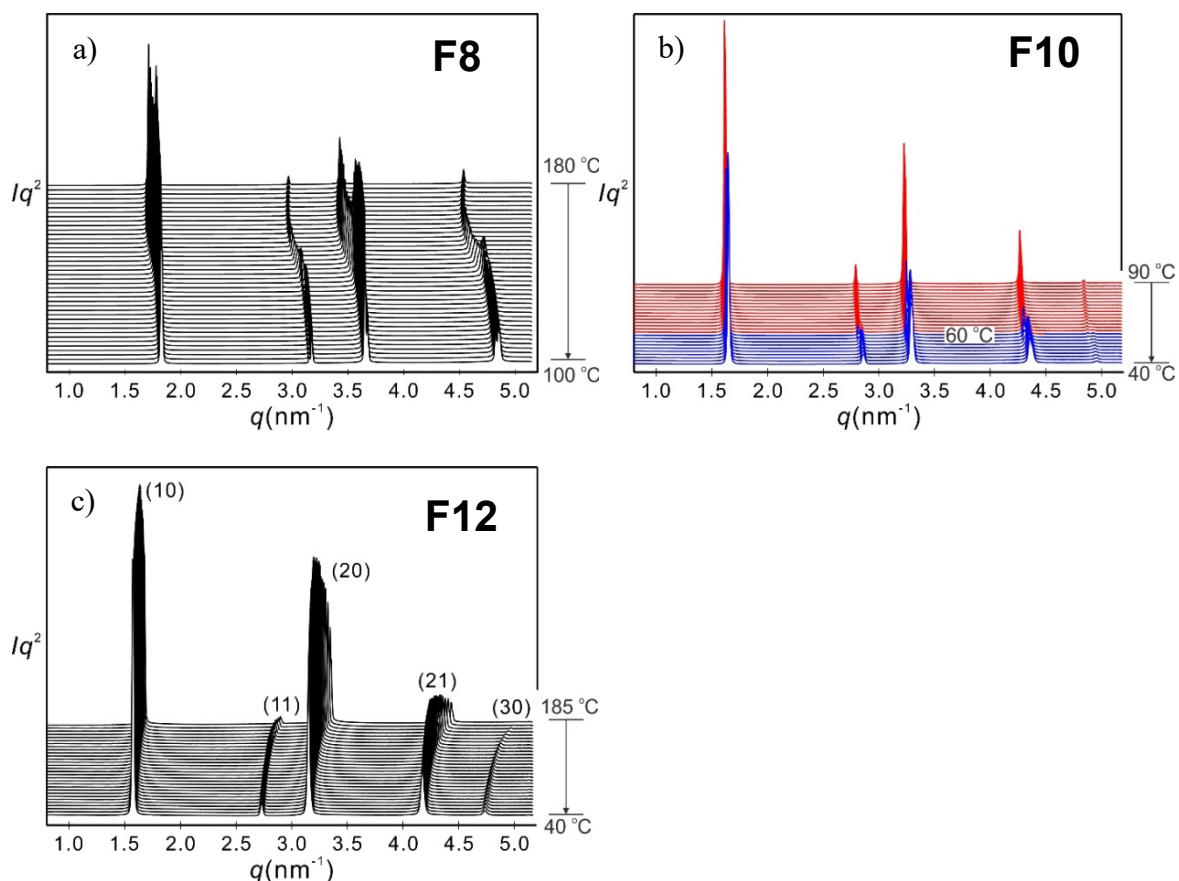


Figure S6. Temperature-dependence of the SAXS diffractograms of selected inner fluorinated compounds **F n** . a-c) T -Scans of the $\text{Col}_{\text{hex}(\Delta)} - \text{Col}_{\text{hex}^T(\Delta)}$ phase transitions of the compound a) **F8**, b) **F10** and c) **F12**.

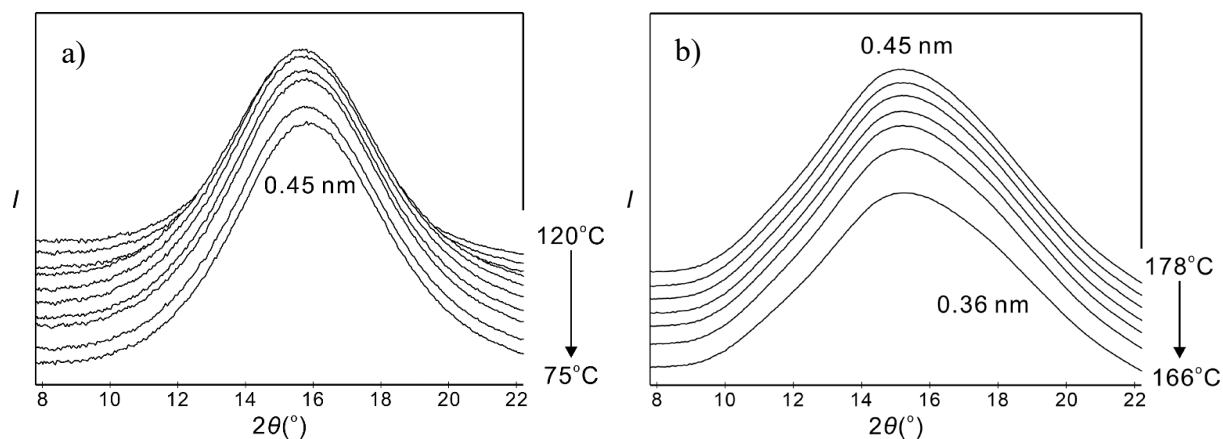


Figure S7. Temperature dependence of the shape of the WAXS diffractograms of compound a) **H6** and b) **F6**.

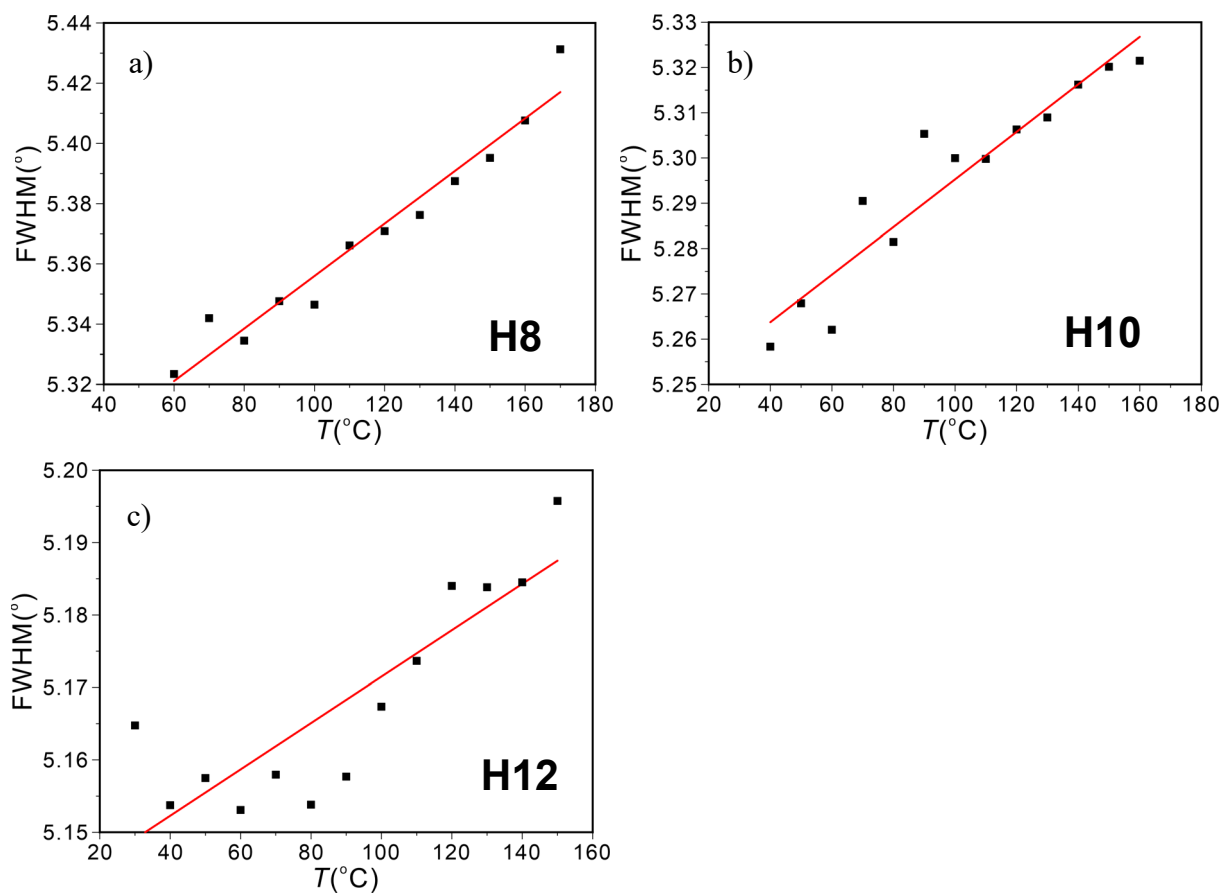


Figure S8. Temperature-dependence of the FWHM of WAXS diffractograms of the compound a) **H8**, b) **H10** and c) **H12**. Red lines represent the fitted curves.

Table S3. XRD data of the $\text{Co}_{\text{hex}(\Delta)}$ phases of compounds **F n** at given temperatures.

Comp.	T (°C)	(hk)		$d_{\text{obs.}}$ (nm)	$d_{\text{cal.}}$ (nm)	intensity	phase	a_{hex} (nm)
F6	175	(10)		3.59	3.59	100.0	0	4.14
		(11)		2.07	2.07	2.2	π	
		(20)		1.79	1.79	6.0	0	
		(21)		1.35	1.36	1.0	π	
F8	140	(10)		3.50	3.50	100.0	0	4.04
		(11)		2.02	2.02	18.2	π	
		(20)		1.75	1.75	68.1	0	
		(21)		1.32	1.32	22.4	π	
F10	130	(10)		3.89	3.89	100	0	4.49
		(11)		2.24	2.25	8.0	π	
		(20)		1.94	1.94	55.9	0	
		(21)		1.47	1.47	10.2	π	
		(30)		1.29	1.30	0.9	0	
F12	120	(10)		3.94	3.94	100.0	0	4.55
		(11)		2.27	2.28	6.7	π	
		(20)		1.97	1.97	64.6	0	
		(21)		1.49	1.49	11.6	π	
		(30)		1.31	1.31	1.5	0	

2.4. Additional ED maps

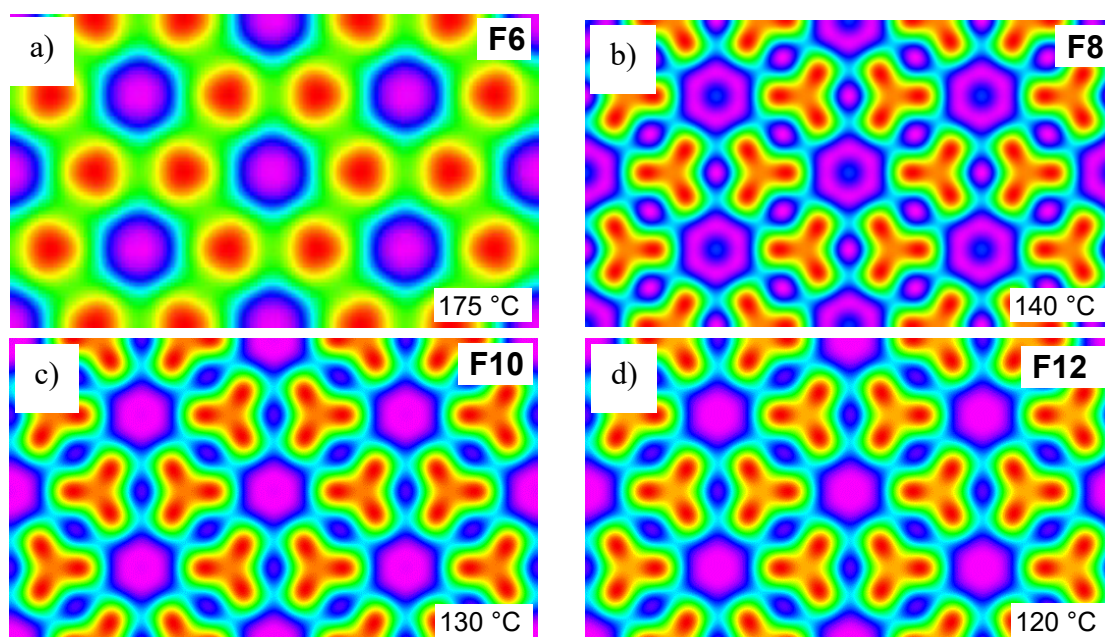


Figure S9. Reconstructed ED maps of the fluorinated compounds **F n** . a) Col_{hex} phase of **F6**, b) Col_{hex}^{T(Δ)} phase of **F8** and c, d) Col_{hex(Δ)} phase of **F10** and **F12**.

3. Determination of structural data

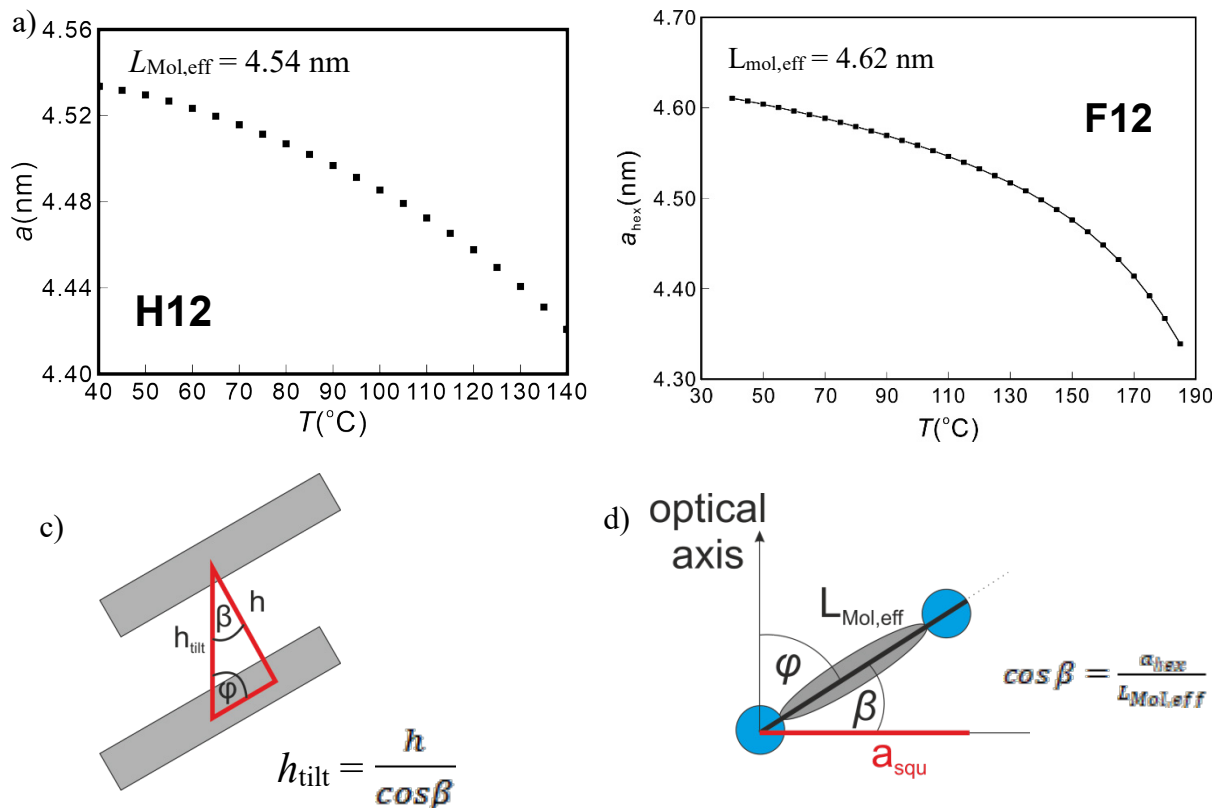


Figure S10. a, b) Determination of the effective molecular length $L_{\text{Mol,eff}}$ of compounds a) **H n** and b) **F n** in the Col_{hex(Δ)}/Col_{hex}^{T(Δ)} phases by extrapolation of the T -scan of the compounds with $n = 12$. c) Determination of the effective height of the prismatic cell h_{tilt} as calculated

from the stacking distance h and the tilt angle β . d) Determination of the tilt angle β of the aromatic cores in the tilted honeycombs.

Table S4. Structural data of the $\text{Col}_{\text{hex}(\Delta)}$ and $\text{Col}_{\text{hex}^T(\Delta)}$ phases of selected compounds **Hn**.^a

Comp.	T [°C]	a_{hex} [nm]	β [°]	h/h_{tilt} [nm]	$V_{\text{mol,cr}}$ [nm ³]	V_{cell} [nm ³]	$n_{\text{cell,LC}}$	n_{wall}
H8	160	4.16	(23.6)	0.45	1.76	6.74	3.42	1.14 ^b
	70 ^T	3.83	32.4	0.53		6.73	3.42	1.14
H10	130	4.35	(16.6)	0.47	1.95	7.70	3.53	1.10 ^b
	40 ^T	3.78	33.6	0.54		6.68	3.06	1.02
H12	130	4.43	(12.6)	0.47	2.15	7.99	3.32	1.11 ^b
	50	4.53	(3.8)	0.44		7.82	3.25	1.08

^a β = Tilt angle of the molecule in the column of the honeycomb phases which was determined with the effective molecular length ($L_{\text{Mol,eff}}$) according to $\cos \beta = a_{\text{hex}}/L_{\text{Mol,eff}}$ (Fig. S9d), the tilt β is uniform in the $\text{Col}_{\text{hex}^T(\Delta)}$ ranges indicated with superscript ^T and shown in bold, or it represents a randomized tilt due to a reduced orientational order parameter in the $\text{Col}_{\text{hex}(\Delta)}$ ranges (shown in brackets); V_{cell} = volume of the unit cell as calculate according to $3^{1/2} a_{\text{hex}}^2/2 \times h'$ with h' in the $\text{Col}_{\text{hex}(\Delta)}$ phases corresponding to the position of the diffuse wide angle scattering maximum around $d = 0.47$ nm and for the uniformly tilted phases calculated using the wide angle scattering around $d = 0.37\text{-}0.38$ nm = h , according to $h' = h_{\text{tilt}} = h/\cos\beta$ (see Fig. S9c); $V_{\text{mol,cr}}$ = volume for a single molecule as calculated using the crystal volume increments;^{S2} n_{cell} = number of molecules in the unit cell, calculated according to $n_{\text{cell}} = 0.893 \times V_{\text{cell}}/V_{\text{mol,cr}}$, where the factor 0.893 is a correction for the reduced packing density in the LC state; $n_{\text{wall}} = n_{\text{cell}}/3$ = average number of molecules in the lateral cross section of the honeycomb walls. ^b Differences to the values given in the ESI in ref S1 result from differences of the used values for h .

Table S5. Structural data of the $\text{Col}_{\text{hex}(\Delta)}$ and $\text{Col}_{\text{hex}^T(\Delta)}$ phases of compounds **Fn**.^a

Comp.	T [°C]	a_{hex} [nm]	β [°]	h/h_{tilt} [nm]	$V_{\text{mol,cr}}$ [nm ³]	V_{cell} [nm ³]	$n_{\text{cell,LC}}$	n_{wall}
F6	175	4.14	(26.3)	0.45	1.60	6.68	3.73	(1.24)
F8	170	4.24	(23.4)	0.47	1.80	7.32	3.63	1.21
	140 ^T	4.04	29.0	0.42		5.94	2.95	0.98
F10	130	4.49	(13.6)	0.47	2.00	8.20	3.66	1.22
	50 ^T	4.41	17.3	0.39		6.57	2.94	0.98
F12	170	4.41	(17.3)	0.46	2.20	7.74	3.14	1.07
	120	4.45	(15.6)	0.46		7.89	3.20	1.07
	50	4.60	(5.3)	0.38		7.00	2.84	0.95

^a For calculations and explanations, see footnote to Table S4.

4. Step-by-step explanation of the self-assembly in the $\text{Col}_{\text{hex}}^{T(\Delta)}$ phase and confirmation of its racemic helix structure

4.1 Analysis of the self-assembly in the $\text{Col}_{\text{hex}}^{T(\Delta)}$ phase

The shrinkage of the lattice parameter a_{hex} of a triangular honeycomb significantly below the molecular length could have different origins:

- 1) A collapse of the triangular honeycomb^{S3}
- 2) Transition from a double- to a single-molecule wall honeycomb^{S4}
- 3) Decrease of the order parameter of the rods and
- 4) A uniform tilt of the molecules in the cylinder walls

In the following the distinct structural models are explained in more detail.

1) A complete collapse of the honeycomb structure, either by loss or reduction of the segregation between polar glycerols and hydrocarbons (alkyls+terphenyls = polar-apolar segregation, as observed for **H6** and **F6**, see Fig. S9a) or between terphenyls and glycerols+alkyls (rigid-flexible segregation), is unlikely to occur upon *lowering* temperature and excluded by the electron density maps which do not change and still show the strict triangular tiling (see Figs. 4m,p and S9b).

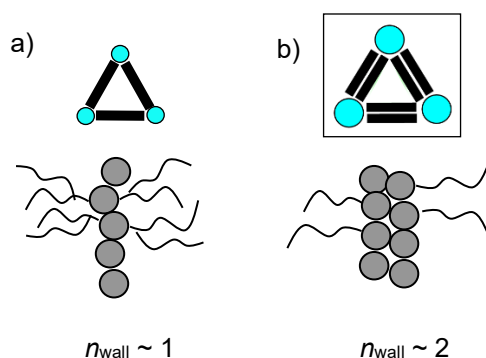


Figure S11. Comparison of single- and double-molecule wall honeycombs. Cross sections through a single triangular prismatic cell with view along the column long axis in direction c (top, blue dots represent the cross sections of the polar columns while black lines represent the rod-like units, the alky chains filling the triangular cell are not shown) and cut through a single honeycomb wall perpendicular to c (bottom, the gray circles represent cuts through the rod-like cores perpendicular to their long axes): a) triangular cell with a single-molecule wall in the lateral cross section and b) back-to-back pairs forming double-molecule walls. If either a) or b) is formed depends on the number and distribution of the lateral chains. T-shaped bolapolyphiles with a single chain form the double-molecule wall structure b), whereas the star shaped polyphiles with branched chains at both sides can only form walls with a single-molecule in the lateral cross section as shown in a).

2) A reduction of the lateral diameter of the honeycomb walls by transition from double- to single-molecule walls would be mainly due to the reduction of the diameter of the glycerol columns, see Fig. S11. In fact, the effective lateral wall diameter is already around only one molecule in the high temperature $\text{Col}_{\text{hex}(\Delta)}$ phase and does not change significantly (n_{wall} , see Tables S4 and S5) in $\text{Col}_{\text{hex}}^T(\Delta)$, because the branched lateral chains at both sides allow only single molecule walls to be formed in both $\text{Col}_{\text{hex}(\Delta)}$ phases. The about 10-20% shrinkage of n_{wall} is mainly a temperature effect, because it takes place irrespectively if there is a $\text{Col}_{\text{hex}(\Delta)}$ - $\text{Col}_{\text{hex}}^T(\Delta)$ phase transition or not (compare **H8**, **H10** with **H12** or **F8** and **F10** with **F12** in Tables S4 and S5). Moreover, in the single-molecule wall structure the parameter a_{hex} should correspond to at least the maximum molecular length ($L_{\text{min}} = 4.4$ nm) due to the significant diameter of the polar columns accommodating 6 glycerols in each 0.45 nm thick raft. Thus, a change of the cylinder wall thickness can be excluded as the origin of lattice shrinkage in $\text{Col}_{\text{hex}}^T(\Delta)$.

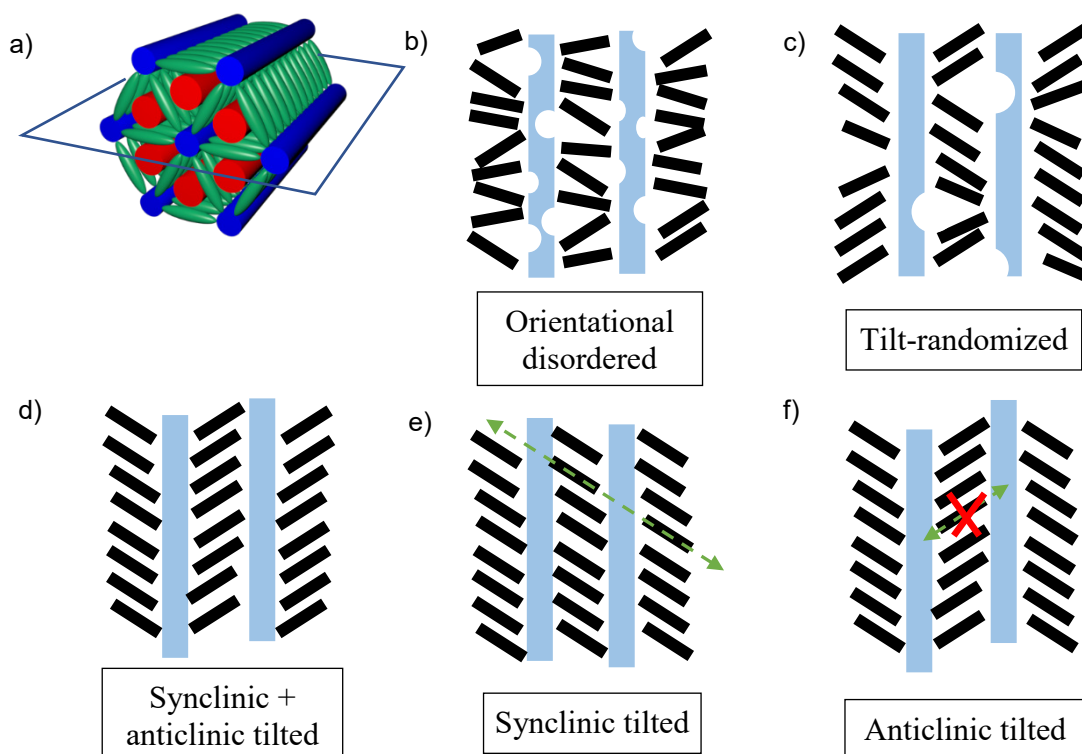


Figure S12. b-e) Different modes of tilt correlation proposed as possible organizations of the rods in the honeycomb walls: three walls, laying in a common plane are shown in b-f) whereas in the 3D model in a) one of the planes is shown for the non-tilted triangular honeycomb. Structures b) and c) are tilt randomized within the individual walls which reduces the order in the cylinder walls and distorts the hydrogen bonding networks in the glycerol columns (blue); the entropic gain is in competition with this enthalpic penalty. The structures d-f) have uniform tilt in the individual walls, but differ in the correlation of the tilt in adjacent walls. This allows the densest core packing and undistorted hydrogen bonding networks along the polar glycerol columns. In d) the tilt correlation between the walls is random, either

synclinc or anticlinc, whereas in e) and f) the tilt correlation between the walls is uniform, either e) synclinc or f) anticlinc. The green dashed arrow in e) indicates the molecular fluctuations taking place parallel to the molecular long axis in the synclinc tilted organization, which provides an entropy gain; this fluctuation is inhibited by the anticlinc layer correlation and reduced in the tilt randomized structures b-d). It is noted that the shown structures can also be found in lamellar (smectic) LC phases of rod-like molecules, where b) and c) represent de Vries type SmA phases e) the synclinc tilted SmC phase and f) the anticlinc SmC_a phase, respectively. The same entropy arguments were used to explain the dominance of SmC over SmC_a phases.^{S5}

3. A decrease of the orientational order parameter of the rod-like units within the cylinder walls would lead to an entropic gain, but would also lead to a local weakening of the hydrogen bonding networks along these columns (Fig. S12b, c) which competes with this entropic gain. The reduced orientational order can occur between individual molecules (Fig. S12b) or between tilt domains with opposite (anticlinc) tilt direction of the molecules along the cylinder walls (Fig. S12c). However, the reduction of the orientational order parameter is unlikely to occur by lowering temperature (Fig. S8) and therefore it should not be the reason for shrinkage of a_{hex} at the Col_{hex(Δ)}-Col_{hex}^{T(Δ)} transition.

4. A uniform (synclinc) tilt of the molecules in the cylinder walls is the only way to efficiently reduce the volume inside the triangular honeycomb without distorting the hydrogen bonding networks (Fig. S12d-f). In adjacent walls the tilt direction can be identical (synclinc, Fig. S12e), opposite (anticlinc, Fig. 12f) or random (Fig. S12d). From smectic LC phases it is known that the synclinc tilt (SmC phases) is favored entropically by the easy fluctuations of the molecules between the layers, which is not possible in the anticlinc SmC_a phase (see Fig 12 d,f).^{S5} Anticlinc (**A**), synclinc (**C**), as well as the tilt-randomized (**B**; syn + anticlinc) structure are shown in panels **A-C** in Fig. S13, where the effect of the tilt correlation on the triangular net structure is shown graphically. The direction of the arrows indicates the direction of tilt, with the arrow pointing out of the plane towards the observer. Because the oligo(p-phenylene ethynylene) unit separating two triangular cells are shared by both adjacent cells (due to the single-molecule wall structure as shown in Fig. S11a) the tilt directions in the walls shared by neighbouring cells has to be uniform. However, the tilt direction of the six walls meeting at each polar column can assume different correlations. A structure with strictly alternating tilt (**A**) can be excluded as it is not commensurate with the trigonal honeycomb structure and would lead to a geometric frustration. It is likely that in the case of predominance of anticlinc tilt correlation alternative structures with reduced symmetry (centred rectangular lattice with $c2mm$ plane group) and involving non-regular triangular cells

are formed, as described previously.⁶ This leaves only the two options **B** and **C** for the organization of the molecules in the triangular honeycombs formed by a tilted organization of the molecules (Fig. S13). In case **B** the tilt direction between the walls is randomized (syn + anticlinic), whereas in case **C** it is uniformly synclenic.

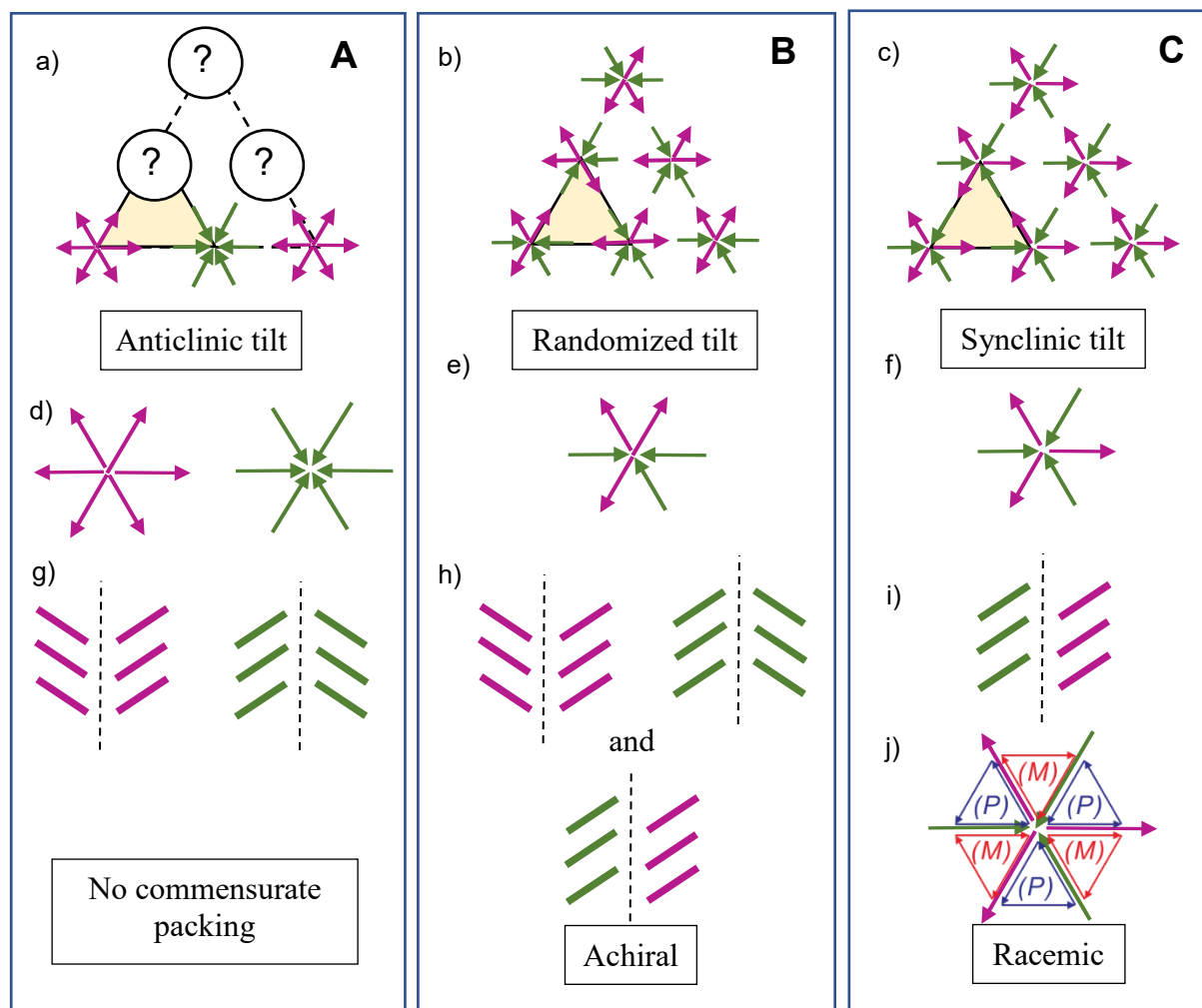


Figure S13. Comparison of the distinct tilt correlations **A-C**: a-f) view along the cylinders; in a-c) on a network section formed by four triangular cells and in d-f) along individual columns; g-i) show a side view on the cylinder walls of two adjacent cells; j) shows the helix sense in the adjacent triangular honeycombs in the synclenic phase (see also Fig. 3e-h). In e) only one of the possible vertex types is shown, the number and orientation of the up/down oriented molecules can assume any possible combination in the tilt randomized structure **B**.

The structure **B** with uniform tilt along each wall, but randomized tilt correlation between the walls involves an equal number of synclenic and anticlinic correlations of the tilt between the walls meeting at the vertices (polar glycerol columns) and allows a commensurate packing in a triangular honeycomb (see Fig. 13b). The tilt randomization between the individual walls is assumed to provide a certain entropic advantage of this structure. However, the presence of

anticlinic tilt correlations restricts the possibility of fluctuations between adjacent cylinder walls.

The structure **C** involves exclusively synclinal tilt correlation within as well as between the walls. This structure might at the first glance be entropically disfavoured with respect to the mixed case **B**. However, the uniformly synclinal tilt correlation allows a higher mobility for the individual molecules by allowing the easy inter-cylinder fluctuation between adjacent walls (see Fig. S12e). The parallel organization of all molecules aligned in one of the three specific directions across all vertices allows fluctuations and translocation of the individual molecules between adjacent cylinders by parallel shifting. This provides an entropic advantage for **C** and a high molecular dynamic is retained despite the long-range periodic structure. On a local scale the synclinal tilted structure is identical with a helical organization of the rods around the triangular prismatic cells with a strictly alternating helix sense between them, as shown in Fig. 3e-h and S13j; there is no alternative option to this racemic helical structure for the synclinal tilted triangular honeycomb.

4.2 Confirmation of the proposed phase structure

Due to the racemic structure it is presently not possible to directly proof the proposed helical structure, as there is no optical activity and also by non-resonant X-ray scattering the helical organization does not show up. Moreover, this structure is formed in a highly dynamic liquid crystalline state where the individual molecules have no fixed positions. This structural dynamic, combined with the small size (0.5 nm for the cylinder wall diameter, < 5 nm for the triangular lattice) makes the direct visualization by the presently accessible nano-scale imaging methods (AFM, STM or TEM) extremely challenging and probably impossible at the present state of technology. However, resonant X-ray scattering could be possibly used to probe the helicity of the structures in this kind and will be the future work of this research.

Though there is no direct proof of the helical structure, optical observation provides a strong support of the hypothesized helical and uniformly synclinal phase structure. The homeotropic aligned sample of the high temperature $\text{Col}_{\text{hex}(\Delta)}$ phase (the columns are perpendicular to the substrate surfaces) appears optically isotropic (dark, see encircled area in Fig. 3c), because the hexagonal phase is optically uniaxial and in the homeotropic alignment the optical axis is parallel to the viewing direction. Upon cooling to $\text{Col}_{\text{hex}}^T(\Delta)$ these homeotropic areas become birefringent (see encircled area in Fig. 3d). The emerging birefringence can be explained by the developing uniform tilt which leads to a tilt of the honeycombs and a transition from a perpendicular to a tilted alignment of the cylinders with respect to the surfaces (the rods tend to keep their alignment parallel to the surfaces, and this requires the tilt of the cylinders). The

tilted cylinders lead to an inclination of the optical axis with respect to the surfaces and this gives rise to the observed birefringence of the previously dark areas at the transition to $\text{Col}_{\text{hex}}^T(\Delta)$ (note that the phase itself remains uniaxial). This change of the optical texture at the phase transition, together with the proven retention of a uniaxial hexagonal lattice at this transition is considered as a proof of the proposed synclinc correlated triangular honeycomb structure. In the case of a random tilt correlation between the walls the average orientation of the columns should not change at the phase transition, at least on the length scale resolvable by the optical investigations, and thus the optical axis should remain parallel to the viewing direction and the homeotropic areas should remain dark.

4.3 Implications for the square honeycombs with tilted molecules

In previous work we reported an analogous square honeycomb phase with tilted organization of the molecules in the cylinder walls ($\text{Col}_{\text{squ}}^T$).^{S7,S8} However, in this case an assignment to a synclinc or anticlinc tilted organization was not possible, because both lead to commensurate structures for a square net. The anticlinc tilt leads to a non-helical structure with alternating up-down organization of the rods around the square prismatic cells, whereas synclinc tilt leads to a racemic helical structure, in this case formed by square cylinders (see Fig. 4 in ref. S7). Based on the knowledge gained herein a uniformly syncline tilted organization in a strictly *P/M*-alternating racemic organization of helical cylinders can be assumed to be the preferred structure in the square honeycombs, too (Fig. 4a in ref. S7). This is supported by a very similar textural change from a dark homeotropic aligned texture to a birefringent homeotropic texture emerging at the $\text{Col}_{\text{squ}} - \text{Col}_{\text{squ}}^T$ phase transition (see Fig. 2 in ref. S7).

5. Discussion of the core-core interactions in **Hn** and **Fn**

The development of tilt is in both series **Hn** and **Fn** mainly a steric effect, determined by the lateral chain volume with respect to the volume available in the triangular prismatic cells. The longitudinal shift of the π -conjugated rods in tilted arrangements is also affected by the electrostatic core-core interactions which change by core fluorination. For compounds **Hn** the electron rich rods preferably assume an edge-to-face organization (Fig. S14a). Collective rotation of the benzene rings in the dynamic LC state leads to a lateral mean distance of $\sim 0.45\text{-}0.48$ nm, being the mean value between the width of 0.68 nm and the face-to-face distance of ~ 0.35 nm^{S9} of the benzene rings and the mean distances between the aliphatic chains and between the glycerols. This edge-to-face organization with a hydrogen bonding between the C-H of the benzenes and the π -faces or π -bonds of the benzenes and acetylene

units of adjacent molecules support a tilt of around 30° (Fig. S14a), being in line with the experimental values.

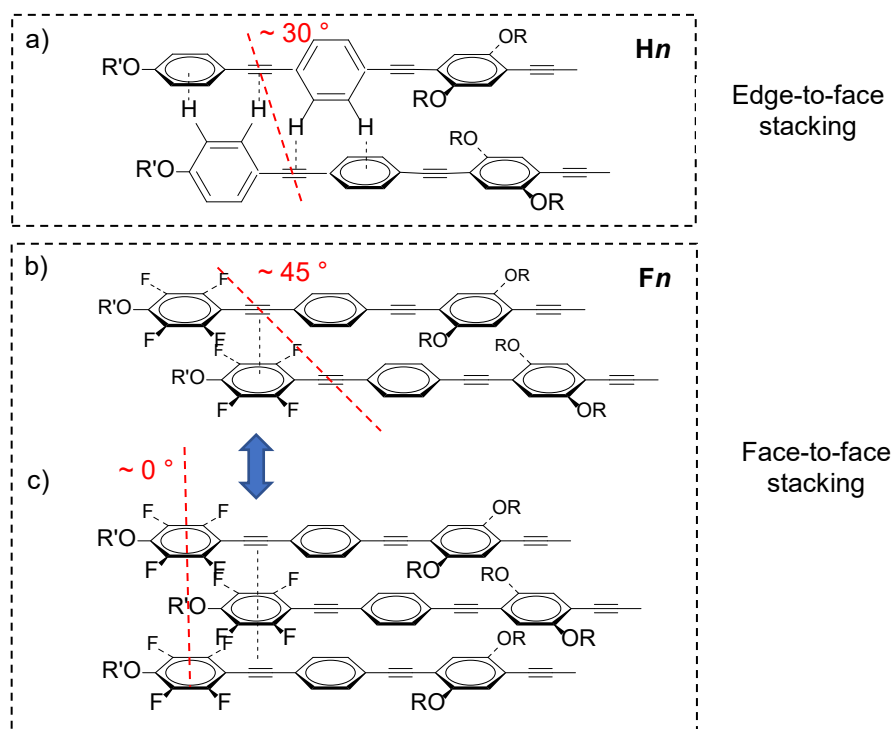


Figure S14. Electrostatic inter-core interactions supporting a longitudinal shift of the π -conjugated cores and thus supporting a tilted organization in the honeycombs of compounds **Hn** and **Fn** with estimated tilt angle.

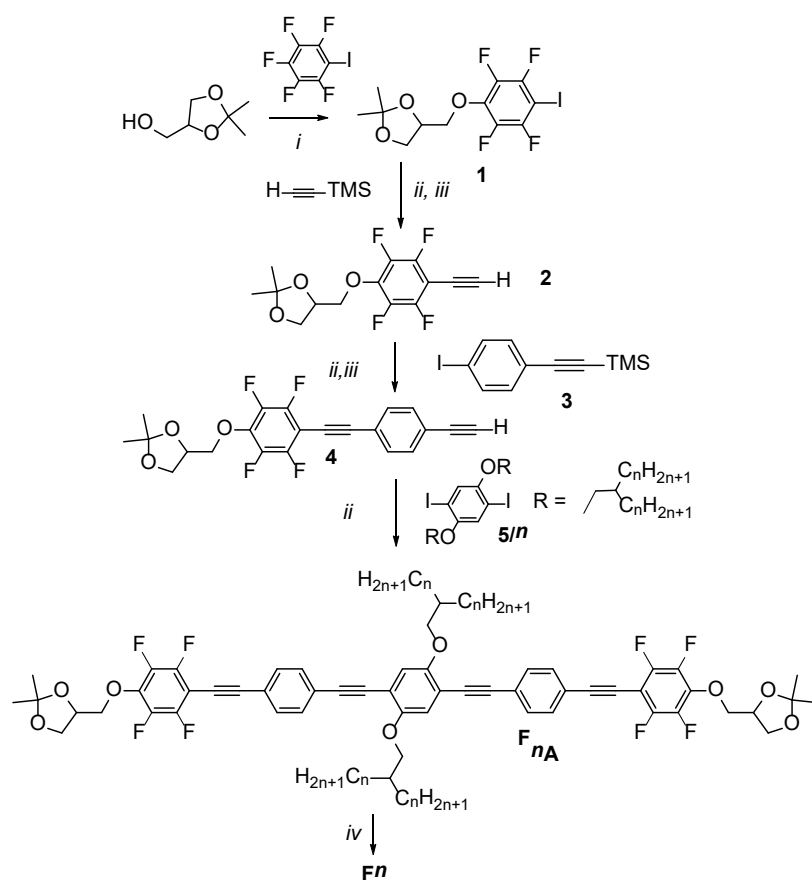
For the fluorinated compound **Fn** this interaction is not possible for all rings (the H-bonding donor sites are removed by H \rightarrow F exchange) and the aspect ratio of the fluorinated benzenes is increased, which supports the face-to-face packing of the benzene rings. This is additionally supported by the strengthening of the electrostatic π - π -stacking interactions either between two fluorinated rings or between the electron deficient perfluoroaromatics and the electron rich acetylenes or non-fluorinated benzenes, respectively (see for example Fig. S14b). The face-to-face stacking allows a denser core packing and restricted rotation around the molecular long axes which leads to the second wide angle scattering maximum around $d = 0.37$ nm.^{S10} Though the donor-acceptor interactions provide a larger displacement and would support a larger tilt, in fact, the tilt becomes smaller for compounds **Fn**. This is explained by the denser core packing achieved by the face-to-face stacking, which at constant side-chain volume decreases the difference between the insufficient chain volume and the excess available cell volume, and thus reduces the driving force for tilt and hence for uniform longitudinal shift. The general increase of a_{hex} by core fluorination suggests that the π -stacking interactions lead to a shift of the rod-like cores with respect to one another, which is not necessarily

uniform and thus allows any tilt angle between 0 and 45° (Fig. S14b↔c), together with a slight increase of a_{hex} upon H→F exchange (see Tables S4, S5).

6. Synthesis and Analytical Data

6.1 General

The general synthesis pathway and the assignment of the compound numbers are given in Scheme S1. The compounds were synthesized from racemic solketal (*rac*-1,2-*O*-isopropylidenedeglycerol) and therefore all compounds **Hn** and **Fn** represent racemic mixtures of diastereomers. 3-[4-(4-Ethynylphenylethynyl)-2,3,5,6-tetrafluorophenyl]-1,2-*O*-isopropylidenedeglycerol (**4**) was synthesized according to the procedures described in the given reference.^[S11] The 2,5-diiodo-1,4-dialkoxybenzenes **5/n** were synthesized according to the procedures given in references^[S1,S12]. The synthesis of the non-fluorinated compounds **Hn** has been described in reference^[S1].



Scheme S1. Synthesis of compounds **F_n**; reagents and conditions: i) K_2CO_3 , DMF, 120 °C, 3 d, 40 °C, 70%, ii) $[\text{Pd}(\text{PPh}_3)_4]$, CuI, NEt_3 , reflux, 6 h, 60 – 95%, iii) K_2CO_3 , $\text{CH}_2\text{Cl}_2/\text{MeOH}$, (2:1), 20 °C, 2 h, 60 – 95%; iv) PPTS, MeOH/THF (1:1), 50 °C, 12 h, 40 – 60%.

The purity of all compounds was checked by thin-layer chromatography (TLC, silica gel 60 F254, Merck). Column chromatography was performed with silica gel 60 (0.063-0.2, Merck), flash-chromatography with silica gel 60 (0.040-0.063, Merck). Triethylamine was distilled from CaH₂ and stored over molecular sieve.

¹H-, ¹³C-NMR spectra (Varian Unity 500 and Varian Unity 400 spectrometers) were recorded in CDCl₃ or pyridine-d₅ solutions, with tetramethylsilane as internal standard). All measurements were operated at 27 °C. Elemental analyses were performed using a Leco CHNS-932 elemental analyzer. Mass spectra were recorded with a Bruker HR-ESI-TOF. The measurements were performed in THF (1 mg/mL) with 0.1 mg/mL LiCl.

6.2 Synthesis procedures and analytical data

6.2.1 General synthetic procedures

P1: Sonogashira cross coupling reaction (ii)^{S 13} : A mixture of 1,4-dialkoxy-2,5-diiodobenzene **5/n** (1 equ.) and the appropriate acetylene **4** (2.1 equ.) was dissolved in dry and purified Et₃N (50 mL for up to 1 mmol). After degassing with argon for 30 min [Pd(PPh₃)₄] (3 mol%) and CuI (2 mol%) were added and the mixture was refluxed for 6 h. After removing the solvent in a rotatory evaporator the obtained residue was purified by column chromatography (eluent: CHCl₃) and used for the next step (**P2**) as received.

P2: Deprotection of the isopropylidene groups with PPTS (iv)^{S 14} : A mixture of the appropriate isopropylidene acetal **FnA** (1 equ.) and PPTS (tip of a spatula) was dissolved in THF/MeOH (1:1, 30 mL for up to 0.5 mmol) and stirred at 50 °C for 12 h. After finishing the reaction the solvent was removed in a rotatory evaporator and the residue solved in DCM. The organic layer was washed with NaHCO₃ solution (3 x 50 mL), water and brine. After drying over Na₂SO₄ the solvent was removed (rotatory evaporator) and the residue purified with column chromatography (eluent: CHCl₃/MeOH, 9:1) and crystallized from MeOH/THF mixtures. The transition temperatures are collated in Table S2.

6.2.2 Synthesis of the acetonides **FnA**

1,4-Bis(2-hexyloct-1-yloxy)-2,5-bis{4-[4-(2,3-*O*-isopropylidene-2,3-dihydroxypropyl-1-oxy)-2,3,5,6-tetrafluorophenylethynyl]phenylethynyl}benzene (F6A**):** Synthesized according to procedure P1 from **5/6** (139 mg, 0.18 mmol), **4** (157 mg, 0.39 mmol),

[Pd(PPh₃)₄] (6.2 mg, 0.005 mmol), CuI (0.7 mg, 0.004 mmol) in NEt₃ (50 mL). Yellow solid, C₇₈H₉₀F₈O₈, *M* = 1306.65 g/mol, mp. 129 °C, yield: 240 mg (98%), ¹H-NMR (400 MHz, CDCl₃) δ 7.59 – 7.50 (m, 8H, Ar-*H*), 7.01 (s, 2H, Ar-*H*), 4.52 – 4.40 (m, 2H, -OCH-), 4.34 (dd, ³*J*(H,H) = 10.2 Hz, ³*J*(H,H) = 5.2 Hz, 2H, -OCH₂-), 4.24 (dd, ³*J*(H,H) = 10.1 Hz, ³*J*(H,H) = 5.6 Hz, 2H, -OCH₂-), 4.16 (dd, ³*J*(H,H) = 8.6 Hz, ³*J*(H,H) = 6.4 Hz, 2H, -OCH₂-), 3.96 (dd, ³*J*(H,H) = 8.6 Hz, ³*J*(H,H) = 5.6 Hz, 2H, -OCH₂-), 3.92 (d, ³*J*(H,H) = 5.7 Hz, 4H, -OCH₂-), 1.90 – 1.79 (m, 2H, -CH-), 1.62 – 1.17 (m, 52H, -CH₂-, -CH₃), 0.86 (t, ³*J*(H,H) = 6.8 Hz, 12H, -CH₃) ppm. ¹⁹F-NMR (376 MHz, CDCl₃) δ -137.56 (td, ³*J*(F,F) = 10.2 Hz, ⁴*J*(F,F) = 3.3 Hz, Ar-*F*), -156.92 (td, ³*J*(F,F) = 9.9 Hz, ⁴*J*(F,F) = 2.9 Hz, Ar-*F*) ppm.

1,4-Bis(2-octyldec-1-yloxy)-2,5-bis{4-[4-(2,3-*O*-isopropylidene-2,3-dihydroxypropyl-1-oxy)-2,3,5,6-tetrafluorophenylethynyl]phenylethynyl}benzene (F8A): Synthesized according to procedure P1 from **5/8** (152 mg, 0.18 mmol), **4** (152 mg, 0.38 mmol), [Pd(PPh₃)₂Cl₂] (3.8 mg, 0.005 mmol), CuI (0.7 mg, 0.004 mmol) in NEt₃ (50 mL). Yellow solid, C₈₆H₁₀₆F₈O₈, *M* = 1418.78 g/mol, mp. 90 °C, yield: 250 mg (98%), ¹H-NMR (400 MHz, CDCl₃) δ 7.58 – 7.49 (m, 8H, Ar-*H*), 7.01 (s, 2H, Ar-*H*), 4.50 – 4.42 (m, 2H, -OCH-), 4.33 (dd, ³*J*(H,H) = 10.1 Hz, ³*J*(H,H) = 5.1 Hz, 2H, -OCH₂-), 4.24 (dd, ³*J*(H,H) = 10.0 Hz, ³*J*(H,H) = 5.6 Hz, 2H, -OCH₂-), 4.16 (dd, ³*J*(H,H) = 8.6 Hz, ³*J*(H,H) = 6.4 Hz, 2H, -OCH₂-), 3.96 (dd, ³*J*(H,H) = 8.6 Hz, ³*J*(H,H) = 5.6 Hz, 2H, -OCH₂-), 3.91 (d, ³*J*(H,H) = 5.6 Hz, 4H, -OCH₂-), 1.89 – 1.82 (m, 2H, -CH-), 1.63 – 1.11 (m, 68H, -CH₂-, -CH₃), 0.86 (t, ³*J*(H,H) = 6.9 Hz, 12H, -CH₃) ppm. ¹⁹F-NMR (376 MHz, CDCl₃) δ -137.57 (td, ³*J*(F,F) = 10.1 Hz, ⁴*J*(F,F) = 3.2 Hz, Ar-*F*), -156.93 (td, ³*J*(F,F) = 9.9 Hz, ⁴*J*(F,F) = 2.9 Hz, Ar-*F*) ppm.

1,4-Bis(2-decyldodec-1-yloxy)-2,5-bis{4-[4-(2,3-*O*-isopropylidene-2,3-dihydroxypropyl-1-oxy)-2,3,5,6-tetrafluorophenylethynyl]phenylethynyl}benzene (F10A): Synthesized according to procedure P1 from **5/10** (160 mg, 0.16 mmol), **4** (135 mg, 0.34 mmol), [Pd(PPh₃)₂Cl₂] (3.6 mg, 0.005 mmol), CuI (0.6 mg, 0.003 mmol) in NEt₃ (50 mL). Yellow solid, C₉₄H₁₂₂F₈O₈, *M* = 1530.90 g/mol, mp. 98 °C, yield: 170 mg (70%), ¹H-NMR (400 MHz, CDCl₃) δ 7.57 – 7.49 (m, 8H, Ar-*H*), 7.00 (s, 2H, Ar-*H*), 4.50 – 4.42 (m, 2H, -OCH-), 4.33 (dd, ³*J*(H,H) = 10.2 Hz, ³*J*(H,H) = 5.1 Hz, 2H, -OCH₂-), 4.24 (dd, ³*J*(H,H) = 10.1 Hz, ³*J*(H,H) = 5.6 Hz, 2H, -OCH₂-), 4.16 (dd, ³*J*(H,H) = 8.6 Hz, ³*J*(H,H) = 6.4 Hz, 2H, -OCH₂-), 3.96 (dd, ³*J*(H,H) = 8.6 Hz, ³*J*(H,H) = 5.6 Hz, 2H, -OCH₂-), 3.91 (d, ³*J*(H,H) = 5.6 Hz, 4H, -OCH₂-), 1.91 – 1.79 (m, 2H, -CH-), 1.62 – 1.16 (m, 84H, -CH₂-, -CH₃), 0.86 (t, ³*J*(H,H) =

6.9 Hz, 12H, $-CH_3$) ppm. ^{19}F -NMR (376 MHz, $CDCl_3$) δ -137.55 (td, $^3J(F,F) = 10.1$ Hz, $^4J(F,F) = 3.2$ Hz, Ar-F), -156.94 (td, $^3J(F,F) = 9.6$ Hz, $^4J(F,F) = 2.6$ Hz, Ar-F) ppm.

1,4-Bis(2-dodecyltetradec-1-yloxy)-2,5-bis{4-[4-(2,3-*O*-isopropylidene-2,3-dihydroxypropyl-1-oxy)-2,3,5,6-tetrafluorophenylethynyl]phenylethynyl}benzene

(F12A): Synthesized according to procedure P1 from **5/12** (135 mg, 0.12 mmol), **4** (100 mg, 0.25 mmol), $[Pd(PPh_3)_4]$ (2.8 mg, 0.004 mmol), CuI (0.5 mg, 0.002 mmol) in NEt_3 (50 mL). Yellow solid, $C_{102}H_{138}F_8O_8$, $M = 1643.03$ g/mol, mp. 96 °C, yield: 160 mg (82%), 1H -NMR (400 MHz, $CDCl_3$) δ 7.57 – 7.49 (m, 8H, Ar-H), 7.00 (s, 2H, Ar-H), 4.50 – 4.42 (m, 2H, $-OCH-$), 4.33 (dd, $^3J(H,H) = 10.1$ Hz, $^3J(H,H) = 5.1$ Hz, 2H, $-OCH_2-$), 4.24 (dd, $^3J(H,H) = 10.0$ Hz, $^3J(H,H) = 5.7$ Hz, 2H, $-OCH_2-$), 4.16 (dd, $^3J(H,H) = 8.5$ Hz, $^3J(H,H) = 6.5$ Hz, 2H, $-OCH_2-$), 3.96 (dd, $^3J(H,H) = 8.6$ Hz, $^3J(H,H) = 5.6$ Hz, 2H, $-OCH_2-$), 3.91 (d, $^3J(H,H) = 5.5$ Hz, 4H, $-OCH_2-$), 1.93 – 1.80 (m, 2H, $-CH-$), 1.62 – 1.12 (m, 100H, $-CH_2-$, $-CH_3$), 0.86 (t, $^3J(H,H) = 6.8$ Hz, 12H, $-CH_3$). ^{19}F -NMR (376 MHz, $CDCl_3$) δ -137.53 (td, $^3J(F,F) = 10.0$ Hz, $^4J(F,F) = 3.1$ Hz, Ar-F), -156.94 (td, $^3J(F,F) = 10.1$ Hz, $^4J(F,F) = 3.1$ Hz, Ar-F) ppm.

6.2.3 Compounds *F_n*

1,4-Bis(2-hexyloct-1-yloxy)-2,5-bis{4-[4-(2,3-dihydroxypropyl-1-oxy)-2,3,5,6-tetrafluorophenylethynyl]phenylethynyl}benzene (F6): Synthesized according to procedure P2 from **F6A** (240 mg, 0.18 mmol) and PPTS (tip of a spatula) in MeOH/THF (1:1, 30 mL:30 mL). Yellow-greenish solid, $C_{72}H_{82}F_8O_8$, $M = 1226.59$ g/mol, yield: 163 mg (73%), 1H -NMR (400 MHz, pyridine- d_5) δ 7.84 – 7.79 (m, 4H, Ar-H), 7.76 – 7.71 (m, 4H, Ar-H), 7.59 (s, 2H, Ar-H, overlapped with solvent signal), 4.90 (dd, $^3J(H,H) = 10.2$ Hz, $^3J(H,H) = 3.9$ Hz, 2H, $-OCH_2-$), 4.80 (dd, $^3J(H,H) = 10.2$ Hz, $^3J(H,H) = 6.3$ Hz, 2H, $-OCH_2-$), 4.61 – 4.52 (m, 2H, $-OCH-$), 4.26 – 4.20 (m, 4H, $-OCH_2-$), 4.12 (d, $^3J(H,H) = 5.5$ Hz, 4H, $-OCH_2-$), 2.06 – 1.94 (m, 2H, $-CH-$), 1.81 – 1.67 (m, 4H, $-CH_2-$), 1.67 – 1.21 (m, 36H, $-CH_2-$), 0.88 (t, $^3J(H,H) = 6.8$ Hz, 12H, $-CH_3$) ppm. ^{19}F -NMR (376 MHz, pyridine- d_5) δ -139.88 – -140.01 (m, Ar-F), -158.04 – -158.17 (m, Ar-F) ppm. ^{13}C -NMR (101 MHz, pyridine- d_5) δ 153.20 ($C_{Ar-Oalkyl}$), 146.18 (m, C_{Ar-F}), 139.85 (m, C_{Ar-F}), 138.30 (m, C_{ArF-O}), 130.97, 130.66 (C_{Ar-H}), 123.63, 120.66 (quart- $C_{Ar}/-C\equiv C-$)^a, 115.86 (C_{Ar-H}), 113.04, 98.73 (quart- $C_{Ar}/-C\equiv C-$)^a, 95.94 (m, quart- C_{ArF}), 93.77, 88.41 ($-C\equiv C-$), 76.34 ($C_{ArF-O-CH_2}$), 75.22 ($-C\equiv C-$), 71.15, 70.54, 62.33 ($-CH-O-$, CH_2O-), 37.19 ($-CH-$), 30.68 30.52, 28.68, 25.83, 21.55 ($-CH_2-$), 12.84 ($-CH_3$) ppm. HRMS (m/z): $[M]+Cl^-$ -calcd. for $C_{72}H_{82}F_8O_8Cl$,

^a In booth regions together in total 3 x quart- C_{Ar} and 1 x $-C\equiv C-$

1261.558; found 1261.552. Anal. Calcd. for $C_{72}H_{82}F_8O_8 \cdot H_2O$: C, 69.44; H, 6.80. Found: C, 69.54; H, 6.74.

1,4-Bis(2-octyldec-1-yloxy)-2,5-bis{4-[4-(2,3-dihydroxypropyl-1-oxy)-2,3,5,6-

tetrafluorophenylethynyl]phenylethynyl}benzene (F8): Synthesized according to procedure P2 from **F8A** (250 mg, 0.17 mmol) and PPTS (tip of a spatula) in MeOH/THF (1:1, 30 mL:30 mL). Yellow-greenish solid, $C_{80}H_{198}F_8O_8$, $M = 1368.76$ g/mol, yield: 173 mg (76%), 1H -NMR (500 MHz, pyridine- d_5) δ 7.85 – 7.80 (m, 4H, Ar-*H*), 7.76 – 7.72 (m, 4H, Ar-*H*), 7.59 (s, 2H, Ar-*H*, overlapped with solvent signal), 4.90 (dd, $^3J(H,H) = 10.2$ Hz, $^3J(H,H) = 4.0$ Hz, 2H, $-OCH_2-$), 4.80 (dd, $^3J(H,H) = 10.1$ Hz, $^3J(H,H) = 6.3$ Hz, 2H, $-OCH_2-$), 4.60 – 4.53 (m, 2H, $-OCH-$), 4.24 – 4.18 (m, 4H, $-OCH_2-$), 4.14 (d, $^3J(H,H) = 5.5$ Hz, 4H, $-OCH_2-$), 2.07 – 1.98 (m, 2H, $-CH-$), 1.82 – 1.71 (m, 4H, $-CH_2-$), 1.68 – 1.58 (m, 4H, $-CH_2-$), 1.58 – 1.17 (m, 48H, $-CH_2-$), 0.90 (t, $^3J(H,H) = 7.0$ Hz, 12H, $-CH_3$) ppm. ^{19}F -NMR (470 MHz, pyridine- d_5) δ -140.25 – -140.39 (m, Ar-*F*), -158.41 – -158.53 (m, Ar-*F*) ppm. ^{13}C -NMR (101 MHz, pyridine- d_5) δ 153.21 (C_{Ar} -Oalkyl), 146.25 (m, C_{Ar} -F), 139.89 (m, C_{Ar} -F), 138.35 (m, C_{ArF} -O), 130.97, 130.67 (C_{Ar} -H), 123.64, 120.67 (quart- $C_{Ar}/-C\equiv C-$)^a, 115.84 (C_{Ar} -H), 113.04, 98.74 (quart- $C_{Ar}/-C\equiv C-$)^a, 96.03 (m, quart- C_{ArF}), 93.77, 88.42 ($-C\equiv C-$), 76.38 (C_{ArF} -O- CH_2-), 75.20 ($-C\equiv C-$), 71.17, 70.53, 62.32 ($-O-CH-$, $-OCH_2-$), 37.21 ($-CH-$), 30.73, 30.54, 29.05, 28.50, 28.25, 25.90, 21.54 ($-CH_2-$), 12.85 ($-CH_3$) ppm. HRMS (m/z): $[M]+Cl^-$ -calcd. for $C_{80}H_{98}F_8O_8Cl$, 1373.683; found 1373.674. Anal. Calcd. for $C_{80}H_{98}F_8O_8 \cdot H_2O$: C, 70.77; H, 7.42. Found: C, 70.87; H, 7.19.

1,4-Bis(2-decyldodec-1-yloxy)-2,5-bis{4-[4-(2,3-dihydroxypropyl-1-oxy)-2,3,5,6-

tetrafluorophenylethynyl]phenylethynyl}benzene (F10): Synthesized according to procedure P2 from **F10A** (170 mg, 0.11 mmol) and PPTS (tip of a spatula) in MeOH/THF (1:1, 30 mL:30 mL). Yellow-greenish solid, $C_{88}H_{116}F_8O_8$, $M = 1480.89$ g/mol, yield: 98 mg (62%), 1H -NMR (400 MHz, pyridine- d_5) δ 7.86 – 7.81 (m, 4H, Ar-*H*), 7.77 – 7.73 (m, 4H, Ar-*H*), 7.59 (s, 2H, Ar-*H*, overlapped with solvent signal), 4.90 (dd, $^3J(H,H) = 10.3$ Hz, $^3J(H,H) = 4.2$ Hz, 2H, $-OCH_2-$), 4.80 (dd, $^3J(H,H) = 10.0$ Hz, $^3J(H,H) = 6.0$ Hz, 2H, $-OCH_2-$), 4.60 – 4.52 (m, 2H, $-OCH-$), 4.24 – 4.18 (m, 4H, $-OCH_2-$), 4.15 (d, $^3J(H,H) = 5.4$ Hz, 4H, $-OCH_2-$), 2.09 – 1.98 (m, 2H, $-CH-$), 1.86 – 1.72 (m, 4H, $-CH_2-$), 1.71 – 1.18 (m, 68H, $-CH_2-$), 0.89 (t, $^3J(H,H) = 6.8$ Hz, 12H, $-CH_3$) ppm. ^{19}F -NMR (376 MHz, pyridine- d_5) δ -138.67 – -138.79 (m, Ar-*F*), -156.85 – -156.98 (m, Ar-*F*) ppm. ^{13}C -NMR (126 MHz, pyridine- d_5) δ 154.35 (C_{Ar} -Oalkyl), 132.16, 131.84 (C_{Ar} -H), 124.81, 121.83 (quart-

$C_{Ar}/-C\equiv C-$)^a, 116.98 ($C_{Ar}-H$), 114.18, 99.91 (quart- $C_{Ar}/-C\equiv C-$)^a, 97.0 (m, quart- C_{ArF}), 94.94, 89.61 ($-C\equiv C-$), 77.54 ($C_{ArF}-O-CH_2-$), 76.38 ($-C\equiv C-$), 72.29, 71.70, 63.48 ($-OCH_2-$), 38.35 ($-CH-$), 31.89, 31.70, 30.22, 29.77, 29.73, 29.70, 29.39, 27.06, 22.69 ($-CH_2-$), 14.01 ($-CH_3$) ppm. HRMS (m/z): [M]+Cl⁻-calcd. for $C_{88}H_{114}F_8O_8Cl$, 1485.808; found 1485.796; Anal. Calcd. for $C_{88}H_{114}F_8O_8\cdot H_2O$: C, 71.91; H, 7.95. Found: C, 72.06; H, 7.91.

1,4-Bis(2-dodecyltetradec-1-yloxy)-2,5-bis{4-[4-(2,3-dihydroxypropyl-1-oxy)-2,3,5,6-tetrafluorophenylethynyl]phenylethynyl}benzene (F12): Synthesized according to procedure P2 from **F12A** (160 mg, 0.10 mmol) and PPTS (tip of a spatula) in MeOH/THF (1:1, 30 mL:30 mL). Yellow-greenish solid, $C_{96}H_{130}F_8O_8$, $M = 1593.01$ g/mol, yield: 60 mg (38%), ¹H-NMR (400 MHz, pyridine-d₅) δ 7.87 – 7.80 (m, 4H, Ar-H), 7.79 – 7.71 (m, 4H, Ar-H), 7.59 (s, 2H, Ar-H, overlapped with solvent signal), 7.15 – 7.08 (br, 2H, -OH), 6.69 – 6.59 (br, 2H, -OH), 4.98 – 4.85 (m, 2H, -OCH₂-), 4.80 (dd, ³J(H,H) = 9.9 Hz, ³J(H,H) = 6.4 Hz, 2H, -OCH₂-), 4.62 – 4.52 (m, 2H, -OCH-), 4.26 – 4.20 (m, 4H, -OCH₂-), 4.16 (d, ³J(H,H) = 5.2 Hz, 4H, -OCH₂-), 2.10 – 1.99 (m, 2H, -CH-), 1.86 – 1.72 (m, 4H, -CH₂-), 1.71 – 1.18 (m, 84H, -CH₂-), 0.89 (t, ³J(H,H) = 6.6 Hz, 12H, -CH₃) ppm. ¹⁹F-NMR (376 MHz, pyridine-d₅) δ -139.82 – -139.99 (m, Ar-F), -158.01 – -158.19 (m, Ar-F) ppm. ¹³C-NMR (101 MHz, pyridine-d₅) δ 153.21 ($C_{Ar}-Oalkyl$), 130.98, 130.68 ($C_{Ar}-H$), 123.66, 120.67 (quart- $C_{Ar}/-C\equiv C-$)^a, 115.86 ($C_{Ar}-H$), 113.05, 98.80 (quart- $C_{Ar}/-C\equiv C-$)^a, 95.62 (m, quart- C_{ArF}), 93.79, 88.46 ($-C\equiv C-$), 78.34 ($C_{ArF}-O-CH_2-$), 76.40 ($-C\equiv C-$), 71.18, 70.53, 62.33 ($-O-CH-$, OCH_2-), 37.21 ($-CH-$), 30.72, 30.55, 29.06, 28.63, 28.60, 28.57 (2C), 28.53, 28.22, 25.90, 21.53 ($-CH_2-$), 12.84 ($-CH_3$) ppm. HRMS (m/z): [M]+Cl⁻-calcd. for $C_{96}H_{130}F_8O_8Cl$, 1597.933; found 1597.923. Anal. Calcd. for $C_{96}H_{130}F_8O_8\cdot H_2O$: C, 72.88; H, 8.41. Found: C, 72.66; H, 8.36.

6.3 Representative NMR-Spectra

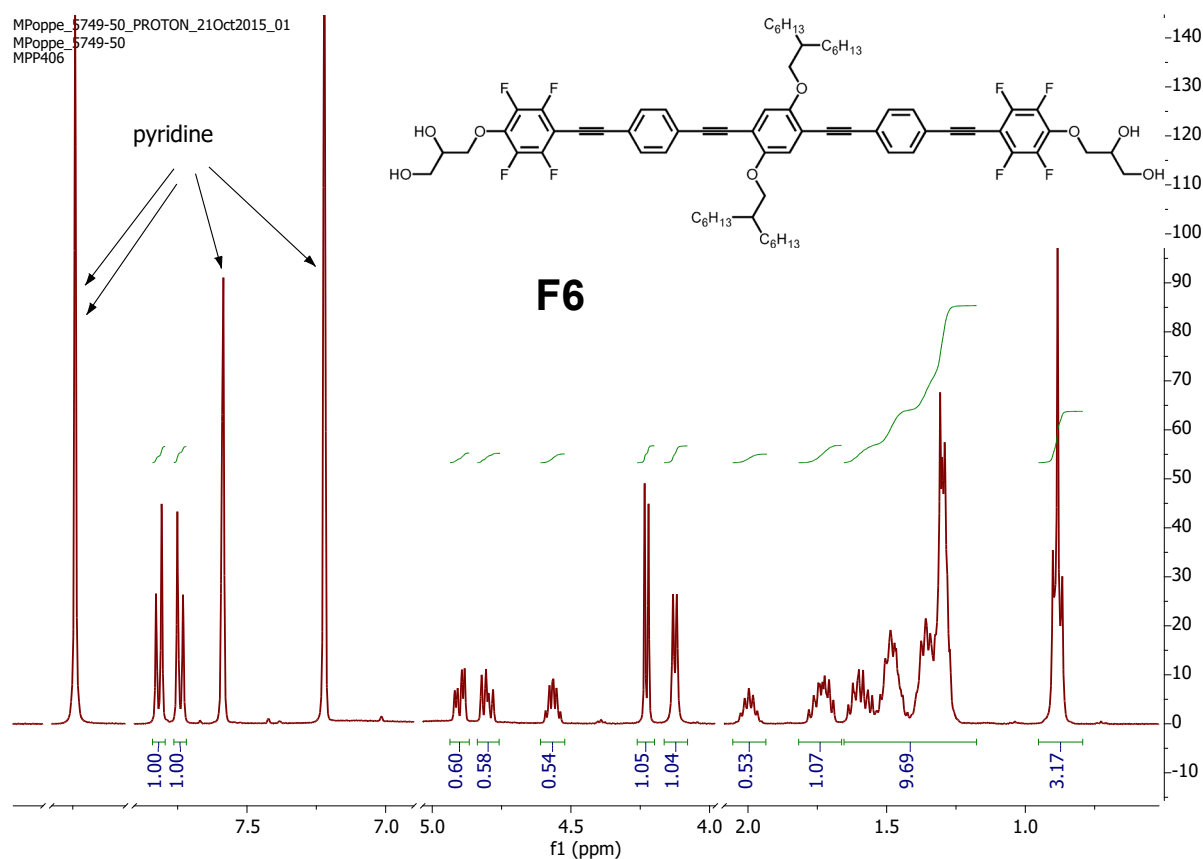


Figure S15. ^1H NMR spectrum of compound **F6** (400 MHz, pyridine- d_5).

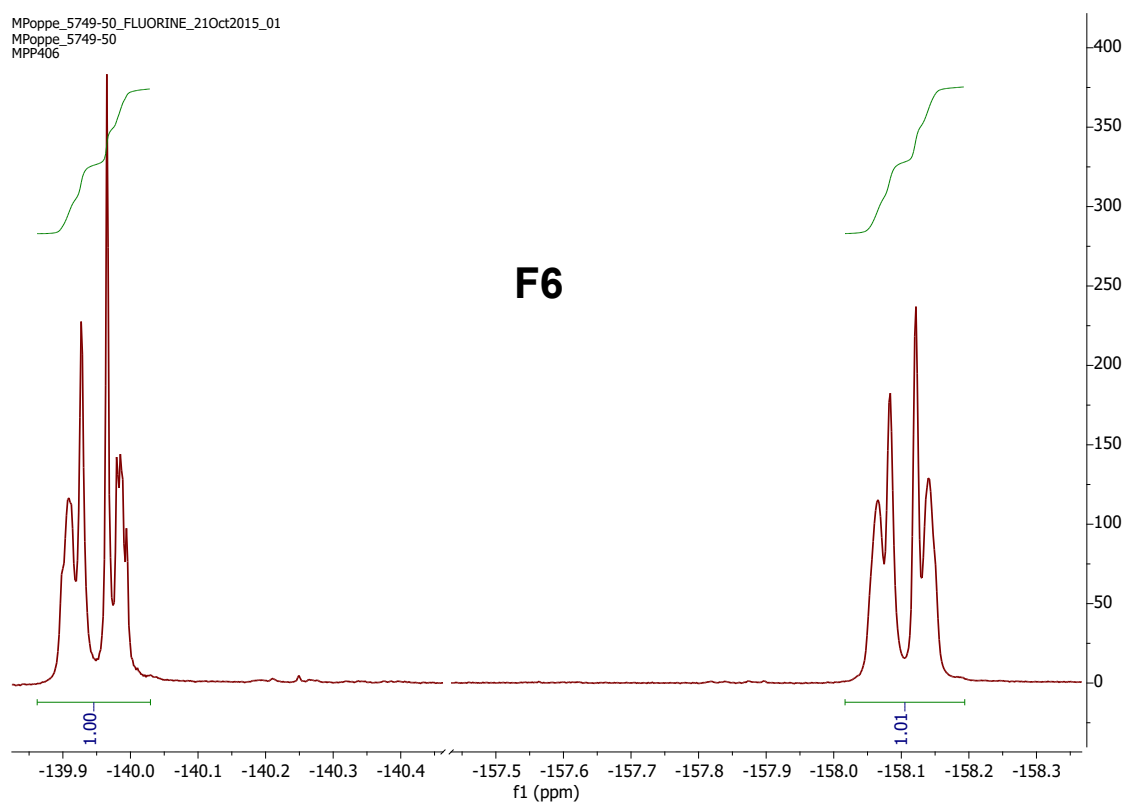


Figure S16. ^{19}F NMR spectrum of compound **F6** (376 MHz, pyridine- d_5).

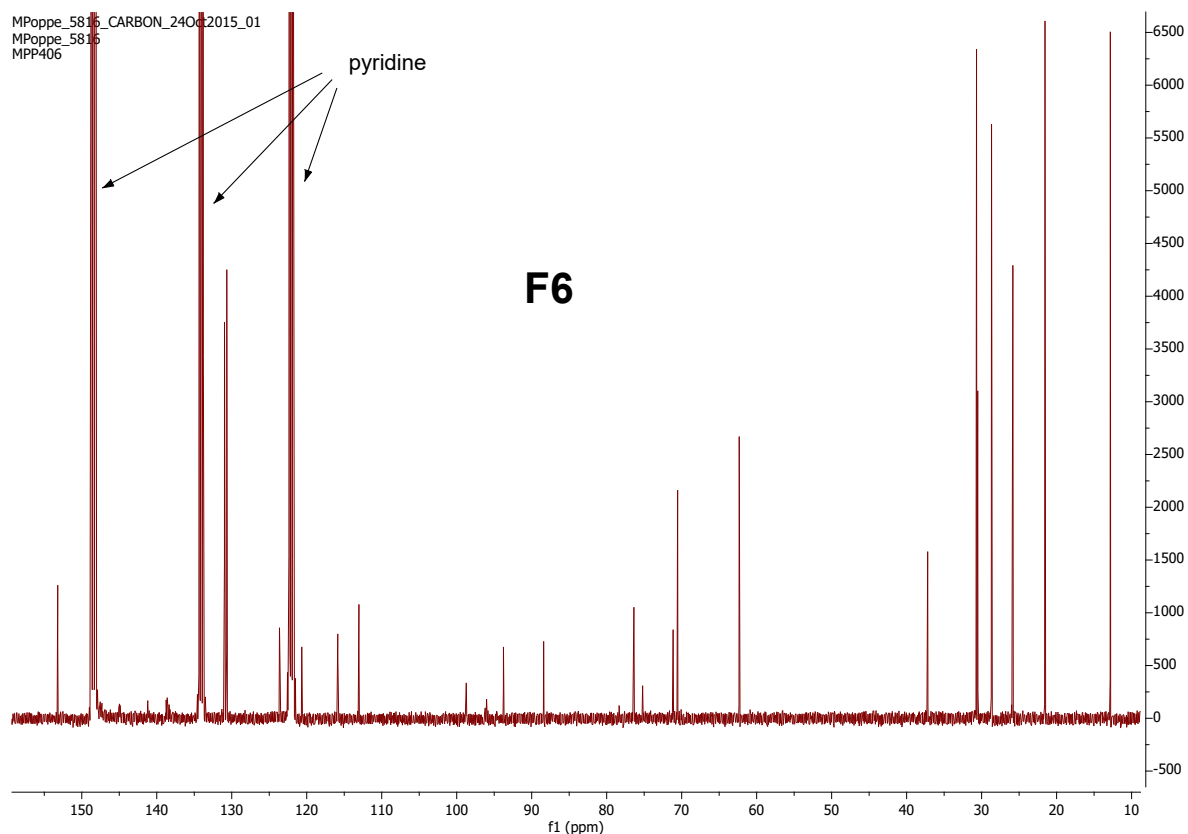


Figure S17. ^{13}C NMR spectrum of compound **F6** (101 MHz, pyridine- d_5).

7. References

- [S1] S. Poppe, M. Poppe, H. Ebert, M. Prehm, C. Chen, F. Liu, S. Werner, K. Bacia, C. Tschierske, *Polymers* 2017, **9**, 471.
- [S2] A. Immirzi, B. Perini, *Acta Cryst. Sect. A* 1977, **33**, 216.
- [S³] S. Poppe, M. Poppe, H. Ebert, M. Prehm, C. Chen, F. Liu, S. Werner, K. Bacia and C. Tschierske, *Polymers* 2017, **9**, 471.
- [S4] Kieffer, R.; Prehm, M.; Glettner, B.; Pelz, K.; Baumeister, U.; Liu, F.; Zeng, X.; Ungar, G.; Tschierske, C. *Chem. Commun.* **2008**, 3861–3863.
- [S5] Y. Lansac, P. K. Maiti, N. A. Clark, M. A. Glaser, *Phys. Rev. E* 2003, **67**, 011703.
- [S6] M. Poppe, C. Chen, S. Poppe, C. Kerzig, F. Liu, and C. Tschierske, *Adv. Mater.* **2020**, 2005070
- [S7] M. Poppe, C. Chen, F. Liu, M. Prehm, S. Poppe and C. Tschierske, *Soft Matter* 2017, **13**, 4676
- [S8] M. Poppe, C. Chen, S. Poppe, F. Liu and C. Tschierske, *Commun. Chem.* 2020, **3**, 70.
- [S9] Levelut, A.-M.; Lambert, M, Structure of B smectic liquid crystals, *Compt. Rend. Acad. Sci.* (Paris) 1971, **272**, 1018.
- [S10] C. A. Hunter and J. K. M. Sanders *J. Am. Chem. Soc.* 1990, **112**, 5525.
- [S11] M. Poppe, C. Chen, F. Liu, S. Poppe, C. Tschierske, *Chem. Eur. J.* 2017, **23**, 7196.
- [S12] M. Poppe, C. Chen, F. Liu, M. Prehm, S. Poppe, C. Tschierske, *Soft Matter* 2017, **13**, 4676.
- [S13] Sonogashira, K.; Tohda, Y.; Hagihara, N.; *Tetrahedron Lett.* 1975, **50**, 4467.
- [S14] R. van Rijsbergen, M.-J. Anteunis, A. de Bruyn, *J. Carbohydr. Chem.* 2006, **2**, 395.